

Contents lists available at ScienceDirect

## Acta Biomaterialia

journal homepage: www.elsevier.com/locate/actbio



### Full length article

# Automated model discovery for textile structures: The unique mechanical signature of warp knitted fabrics



Jeremy A. McCulloch, Ellen Kuhl\*

Department of Mechanical Engineering, Stanford University, Stanford, California, United States

#### ARTICLE INFO

Article history:
Received 26 July 2024
Revised 21 September 2024
Accepted 26 September 2024
Available online 3 October 2024

Keywords:
Textile structures
Knitted fabrics
Biaxial testing
Constitutive modeling
Anisotropy
Constitutive neural networks
Machine learning

#### ABSTRACT

Textile fabrics have unique mechanical properties, which make them ideal candidates for many engineering and medical applications: They are initially flexible, nonlinearly stiffening, and ultra-anisotropic. Various studies have characterized the response of textile structures to mechanical loading; yet, our understanding of their exceptional properties and functions remains incomplete. Here we integrate biaxial testing and constitutive neural networks to automatically discover the best model and parameters to characterize warp knitted polypropylene fabrics. We use experiments from different mounting orientations, and discover interpretable anisotropic models that perform well during both training and testing. Our study shows that constitutive models for warp knitted fabrics are highly sensitive to an accurate representation of the textile microstructure, and that models with three microstructural directions outperform classical orthotropic models with only two in-plane directions. Strikingly, out of 214 = 16,384 possible combinations of terms, we consistently discover models with two exponential linear fourth invariant terms that inherently capture the initial flexibility of the virgin mesh and the pronounced nonlinear stiffening as the loops of the mesh tighten. We anticipate that the tools we have developed and prototyped here will generalize naturally to other textile fabrics-woven or knitted, weft knit or warp knit, polymeric or metallic-and, ultimately, will enable the robust discovery of anisotropic constitutive models for a wide variety of textile structures. Beyond discovering constitutive models, we envision to exploit automated model discovery as a novel strategy for the generative material design of wearable devices, stretchable electronics, and smart fabrics, as programmable textile metamaterials with tunable properties and functions. Our source code, data, and examples are available at https://github.com/LivingMatterLab/CANN.

### Statement of significance

Textile structures are rapidly gaining popularity in many biomedical applications including tissue engineering, wound healing, and surgical repair. A precise understanding of their unique mechanical properties is critical to tailor them to their specific functions. Here we integrate mechanical testing and machine learning to automatically discover the best models for knitted polypropylene fabrics. We show that warp knitted fabrics possess a complex symmetry with three distinct microstructural directions. Along these, the behavior is dominated by an exponential linear term that characterize the initial flexibility of the virgin mesh and the nonlinear stiffening as the loops of the fabric tighten. We expect that our technology will generalize naturally to other fabrics and enable the robust discovery of complex anisotropic models for a wide variety of textile structures.

© 2024 The Author(s). Published by Elsevier Ltd on behalf of Acta Materialia Inc.

This is an open access article under the CC BY-NC-ND license (http://creativecommons.org/licenses/by-nc-nd/4.0/)

### 1. Motivation

Synthetic meshes have unique mechanical properties [3], which make them ideal candidates for many engineering and medical applications [19]: Under small deformations they display a remarkable *initial flexibility*, under large deformations, they exhibit a pro-

<sup>\*</sup> Corresponding author.

E-mail address: ekuhl@stanford.edu (E. Kuhl).

nounced nonlinear stiffening, and under varying loading scenarios, they reveal an ultra-anisotropic response [18]. Their compliant nature allows them to effortlessly undergo large deformations while maintaining structural integrity [9]. Their inherent porosity encourages fluid flow and nutrient exchange, crucial for many biological or technical functions [41]. Their anisotropic nature enables them to adapt and function effectively in complex dynamic environments [38]. Collectively, these unique features make meshes highly suitable for a range of biomedical applications, including surgical repair, drug delivery, wound healing, implant design, and tissue engineering [37]. Beyond biomedicine, meshes are becoming increasingly popular in other technical applications including filtration systems, protective gear, flexible electronics, and structural reinforcement [29].

The microstructure of the mesh is critical to its function. The mechanical properties of the mesh directly affect how well it integrates within its environment, distributes stresses, and provides structural support [7]. In fabric mechanics, we distinguish two fundamentally different types of meshes: woven and knitted [18]. The microstructure of woven fabrics consists of warp threads running lengthwise and shute or weft threads running widthwise. The shute threads are woven over and under the warp threads interlacing them at right angles to create a tight and stable grid-like pattern with two orthogonal microstructural directions, the warp direction  $\boldsymbol{w}$  and the shute direction  $\boldsymbol{s}$ . Along these directions, woven fabrics are rather stiff; off-set at 45 degrees, they are fairly compliant, meaning they have a high tensile stiffness, but a low shear stiffness [44]. The microstructure of knitted fabrics consists of interlocking loops of yarn, creating a flexible and stretchable textile structure that can easily adapt its shape and undergo large deformations while maintaining structural integrity [24]. We distinguish two families of knitted structures: weft-knitted and warp knitted [21]. The microstructure of weft knitted fabrics consists of horizontal rows of interlocking loops. It is made by looping a single varn back and forth horizontally across the fabric width, creating interconnected loops, row by row, with two orthogonal microstructural directions, the production or wale direction  $\boldsymbol{w}$  and the varn direction s. Regardless of the direction of loading, weft knitted fabrics tend to be extremely extensible and dimensionally unstable [55]. The microstructure of warp knitted fabrics consists of vertical columns of interlocking loops. It is made by looping multiple parallel yarns vertically along the fabric length, zigzagging between two neighboring columns, creating interconnected loops, column by column, with the production or warp direction  $\vec{w}$  and one or multiple yarn directions  $\mathbf{s}_{l}$  and  $\mathbf{s}_{ll}$ . In the warp direction, warpknitted fabrics are fairly stiff; in the yarn directions, the stiffness is tunable by the interlocking pattern [50]. Of the three different microstructures in Fig. 1, warp knitted structures are the most tunable: The design space of a single loop spans  $3 \times 2 \times 3 = 18$  possibile configurations, three for the incoming yarn, two for the loop itself-open or closed-, and three for the outgoing yarn [21]. For warp knitted structures made with two guide bars, this already results in  $18 \times 18 = 324$  possible combinations, and modern knitting machines have four or more guide bars. This opens tremendous opportunities to design warp knitted fabrics with mechanicallyguided microstructures and custom-designed properties [4].

Synthetic meshes play an integral role in surgical repair. Initially introduced for hernia repair in the 1950s, the primary goal of synthetic meshes is to reinforce weakened or damaged structures and provide durable structural integrity. Hernia repair is a common surgery, with more than 20 million procedures each year [54]. In spite of this high prevalence, complications are relatively common, with 11 percent of patients reporting postoperative abdominal pain [42]. Hernia repairs use various methods to close the wound in the abdominal wall, but the most common surgical in-

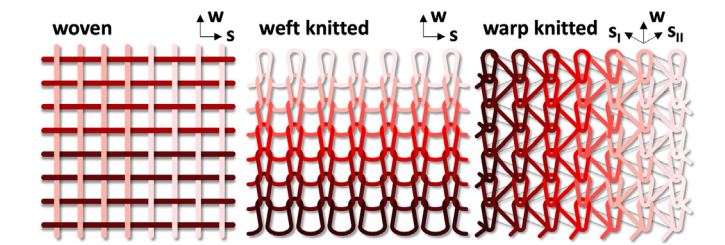


**Fig. 1.** Microstructure of woven, weft and warp knitted fabrics. Woven fabrics consist of a series of parallel warp strands alternately passed over and under by a set of parallel shute strands creating a microstructure with two orthogonal directions, the warp direction  $\boldsymbol{w}$  and the shute direction  $\boldsymbol{s}$ . Knitted fabrics consists of continuous filaments that are looped around one another. Weft knitted fabrics consists of horizontal rows of interlocking loops creating a microstructure with two orthogonal directions, the production or wale direction  $\boldsymbol{w}$  and the yarn direction  $\boldsymbol{s}$ . Warp knitted fabrics consists of vertical columns of interlocking loops creating a microstructure with a warp direction  $\boldsymbol{w}$  and one or more yarn directions  $\boldsymbol{s}_l$  and  $\boldsymbol{s}_{ll}$ .

tervention is to suture a synthetic mesh over the wound [53]. In addition to the surface properties of the mesh at the mesh tissue interface that determine the durability of the reconstruction [23], it is essential that the surgeon selects a mesh with appropriate size, suture factors, and biomechanical properties [40]. A mismatch between the mechanics of the mesh and the surrounding tissue can increase the risk of postoperative failure [7]. To assess the mechanical biocompatibility of a synthetic mesh, we must understand its mechanical properties [13]. Thus, there is a critical need to develop constitutive models for synthetic meshes to better understand how they interact with the surrounding tissue [31]. Here, as a first step, we limit this understanding to the hyperelastic regime, and do not consider dynamic [20] or frictional [39] effects. Within this regime, previous studies have performed biaxial testing of various mesh patches [9]; however, these studies only extracted a few phenomenological parameters and did not combine data from multiple experiments into a unified mechanistic constitutive model. The benefit of obtaining a fully three-dimensional hyperelastic constitutive model from experimental data is that such a model would describe the stress state of the mesh induced by any possible deformation, including complex states that we do not test experimentally, but may well occur in vivo [51]. However, here we will not follow the traditional approach, propose yet another phenomenological model, and fit its parameters to data. Instead, our objective is to discover a microstructurally motivated hyperelastic constitutive model for warp-knitted fabrics and establish a robust set of experimental and computational techniques to autonomously discover the best constitutive models and parameters for a variety of woven, weft and warp knitted textile structures and other synthetic microstructural materials.

Constitutive modeling requires deep expert knowledge. A constitutive model aims to predict the internal stress state of a material as a function of its strain. In particular, in developing elastic constitutive models, we assume that the Piola stress tensor is a function of the deformation gradient tensor [17]. There are various approaches to infer this relationship between the deformation gradient and the Piola stress from mechanical testing data. Classical approaches attempt to fit a few unknown parameters of wellknown phenomenological models such as the neo Hooke model [60], the Lanir model [22], or the Demiray model [8]. The challenge with this approach is that it requires a profound domain expertise to select an appropriate model, and we may need to repeat model selection and parameter identification several times to identify a model that fits the data well. Constitutive neural networks use physics-informed insights about constitutive models as well as powerful deep learning methods to simultaneously discover

the function form of the constitutive model and learn its appropriate parameters [26]. While the first family of constitutive neural networks only discovered isotropic models for materials such as rubber [26], brain [27] or plant-based meat [47], more recent networks can now discover transversely isotropic models for skin [28] or arteries [45]. Here we explore how to expand constitutive neural networks to discover more complex anistropic constitutive models from biaxial extension data.

Constitutive neural networks can autonomously discover the best model and parameters. A constitutive neural network is a machine learning model that takes the deformation gradient as an input and outputs the Piola stress for a specific material [25]. Constitutitve artificial neural networks take advantage of physical laws and assumptions about the material to constrain the inputoutput relationship that the network discovers, similar to physicsinformed neural networks [49]. However, constitutive neural networks differ from physics-informed neural networks, which alter the loss function to satisfy physical laws. Instead, constitutive neural networks modify the architecture of the underlying machine learning model such that, regardless of the model parameters, the discovered model exactly satisfies the relevant physical laws [26]. The particular assumptions that motivate the design of hyperelastic constitutive neural networks are material objectivity, thermodynamic consistency, incompressibility, and material symmetry. Prior work has enforced various forms of symmetry including isotropy [26], transverse isotropy [28], and orthotropy [30]; here we assume that warp-knitted meshes have either two or three characteristic microstructural orientations in the plane of the mesh. Unlike most previous work that trains anisotropic constitutive neural networks exclusively by using homogeneous tests [58], we explore how to use biaxial testing data when neither of the loading axes are aligned with the symmetry planes of the material [52]. We acknowledge that this violates the condition of homogeneity; yet, it allows us to train our network with a broader class of deformations, and discover models that are more robust when predicting stresses in response to deformation states that the network has not previously seen during training [59]. Finally, while constitutive neural networks are able to discover constitutive models by selecting from a large set of possible strain energy functions, the most useful constitutive models have only a small number of parameters and are therefore interpretable [5]. Various regularization techniques can help reduce the number of non-zero parameters without significantly sacrificing model accuracy [14]. Prior work has shown that, when computationally tractable,  $L_0$  regularization is the best method for identifying the optimal n-term model for a fixed, small n [32]. When n is too large for  $L_0$  optimization,  $L_p$ regularization with 0 can effectively reduce the number ofnon-zero terms [46], without significantly decreasing model accuracy [12]. Here we will apply both approaches, compare the discovered models, and make recommendations which regularization to choose.

### 2. Methods

### 2.1. Experimental methods

We prepared samples from a 0.5 mm thick warp knitted surgical mesh of extruded polypropylene designed for surgical repair (PROLENE® Ethicon, Inc., Somerville, NJ), to test under biaxial loading in a CellScale BioTester 5000. We define the *warp direction* of the mesh as the direction along which the loops are aligned, which is also the direction in which the mesh is stiffest.

We then define the *shute directions* in the plane of the mesh, either as one direction orthogonal to the warp direction inclined by 90 degrees, or as two directions symmetrically inclined to the warp

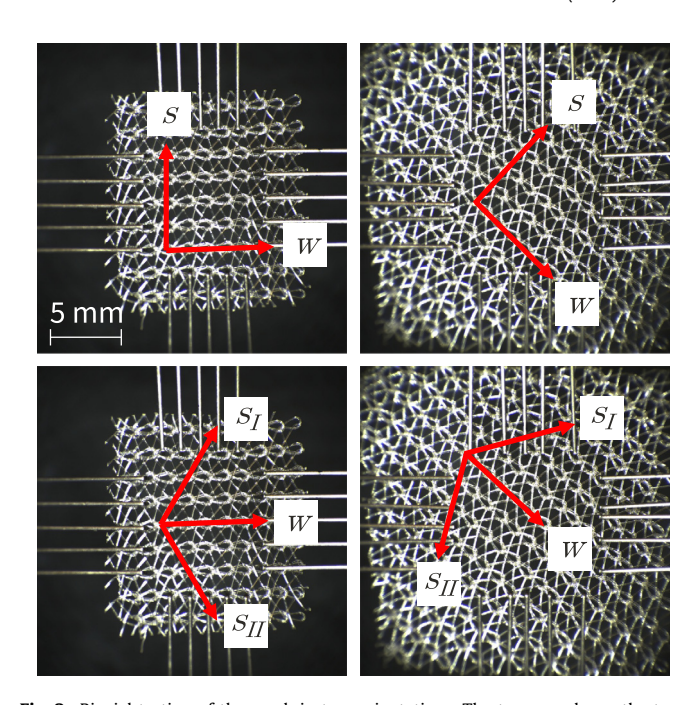


**Fig. 2.** Biaxial testing of the mesh in two orientations. The top row shows the twofiber model with one warp and one shute direction  $\mathbf{w}$  and  $\mathbf{s}$ , and the bottom row shows the three-fiber model with one warp and two shute directions  $\mathbf{w}$  and  $\mathbf{s}_1$  and  $\mathbf{s}_1$ . The left column illustrates the mesh in the 0/90 or 0/+60/-60 orientations, and the right column illustrates the mesh in the -45/+45 or -45/+15/+75 orientations.

direction by 60 degrees. We cut the mesh into square sections two different orientations: In the first orientation, which we denote as the 0/90 orientation or 0/+60/-60 orientation, the sample is aligned with the warp direction; in the second orientation, which we denote as the -45/+45 orientation or -45/+15/+75 orientation, the sides of the sample are 45 degrees offset from the warp direction. Fig. 2 illustrates the samples of each orientation, mounted into the testing device. In the 0/90 or 0/+60/-60 orientation, in the left column, we place the tines of the biaxial testing device in the loops of the mesh. To prevent the mesh from unravelling, we avoid placing the tines in the row of loops that is closest to the edge of the sample. In the -45/+45 or -45/+15/+75 orientation, in the right column, we place the tines in the loops of the mesh where feasible, but due to the geometry of the mesh not all tines fit exactly into a loop. To reduce the likelihood of unraveling, we use a larger mesh area in this orientation.

We test a total of ten samples, five for each orientation [10]. Once we mount each sample into the device, we apply a 30 mN preload along both axes to establish a consistent reference configuration [61]. After preloading, we record the spacing between the tines as the gauge length, and perform five consecutive tests with 30 seconds of rest between each test [33]. Each test consists of linearly increasing the applied stretch for 100 seconds, followed by linearly decreasing the applied stretch for 100 seconds until the sample returns to its unstretched state. Table 1 summarizes the maximum stretches in each direction for each of the five tests. We perform all five tests on each of the ten samples. However, to minimize the effect of preload, we randomize the order of the tests for each sample.

#### 2.2. Stress and strain analysis

We process the data from the CellScale BioTester 5000 to obtain the average Piola stress for given stretch values  $\lambda_1$  and  $\lambda_2$ . First, we convert the force and displacement measurements to stresses and stretches. To do so, we measured the sample thickness t with

Table 1

Definition of five biaxial test settings. Maximum stretches  $\lambda_1$  and  $\lambda_2$  for the five different tests of each sample. We increase the stretch linearly for 100 seconds until reaching the maximum stretch for each test, then decrease it linearly for 100 seconds to the undeformed configuration, and hold the sample in the undeformed configuration for 30 seconds between consecutive tests. To minimize the effect of preload, we randomize the order of the tests for each sample.

experiment	max stretch $\lambda_1$	max stretch $\lambda_2$
strip-x	1.10	1.00
off-x	1.10	1.05
equibiax	1.10	1.10
off-y	1.05	1.10
strip-y	1.00	1.10

calipers and set the gauge lengths  $L_1$  and  $L_2$  to the initial spacing between the tines in the 1- and 2-directions. Then, we computed the stretches  $\lambda_1$  and  $\lambda_2$  and the Piola stresses  $P_{11}$  and  $P_{22}$ ,

$$\lambda_1 = \frac{l_1}{L_1}$$
  $\lambda_2 = \frac{l_2}{L_2}$   $P_{11} = \frac{F_1}{L_2 t}$   $P_{22} = \frac{F_2}{L_1 t}$  (1)

where  $l_1$  and  $l_2$  are the measured gauge lengths and  $F_1$  and  $F_2$  are the measured forces in the 1- and 2-directions. The result are five loading and five unloading curves for each of the ten samples. We resample and average all curves at equidistant stretch intervals to obtain an averaged stress pair  $\{P_{11}, P_{22}\}$  for each stretch pair  $\{\lambda_1, \lambda_2\}$ . Finally, for the samples mounted in the -45/+45 orientation, we use symmetry with respect to the diagonale and average the ten recorded stress-stretch curves to five distinct curves.

### 2.3. Kinematics

We characterize the deformation through the mapping  $\mathbf{x} = \varphi(\mathbf{X})$  that maps a point  $\mathbf{X}$  in the reference configuration to a point  $\mathbf{x}$  the deformed configuration. We then describe the local deformation using the deformation gradient,

$$\mathbf{F} = \nabla_{\mathbf{X}} \boldsymbol{\varphi}(\mathbf{X}) \,. \tag{2}$$

Multiplying F with its transpose  $F^t$  introduces the symmetric right Cauchy Green deformation tensor C,

$$\mathbf{C} = \mathbf{F}^{\mathsf{t}} \cdot \mathbf{F} \,. \tag{3}$$

To characterize the deformation of an orthotropic material, we introduce the three isotropic invariants,  $I_1$ ,  $I_2$ ,  $I_3$ , and a set of anisotropic invariants,  $I_{4i}$ ,  $I_{8ij}$  [35,56],

$$\begin{array}{lll} I_1 &= [\mathbf{F}^t \cdot \mathbf{F}] : \mathbf{I} & \partial_{\mathbf{F}} I_1 &= 2\mathbf{F} \\ I_2 &= \frac{1}{2} [I_1^2 - [\mathbf{F}^t \cdot \mathbf{F}] : [\mathbf{F}^t \cdot \mathbf{F}]] & \partial_{\mathbf{F}} I_2 &= 2I_1\mathbf{F} - 2\mathbf{F} \cdot \mathbf{F}^t \cdot \mathbf{F} \\ I_3 &= \det(\mathbf{F}^t \cdot \mathbf{F}) = J^2 & \partial_{\mathbf{F}} I_3 &= \det(\mathbf{F}) \, \mathbf{F}^{-t} \\ I_{4i} &= [\mathbf{F}^t \cdot \mathbf{F}] : [\vec{n}_i \otimes \vec{n}_i] & \partial_{\mathbf{F}} I_{4i} &= 2\mathbf{F} \cdot [\vec{n}_i \otimes \vec{n}_i] \\ I_{8ij} &= [\mathbf{F}^t \cdot \mathbf{F}] : [\vec{n}_i \otimes \vec{n}_j]^{\mathrm{sym}} & \partial_{\mathbf{F}} I_{8ij} &= 2\mathbf{F} \cdot [\vec{n}_i \otimes \vec{n}_j]^{\mathrm{sym}} \end{bmatrix}, \end{array} \tag{4}$$

where I is the identity tensor,  $n_{i,j}$  with  $i,j=1,\ldots,n_{\rm dir}$  are the unit warp and shute directions in the undeformed reference configuration, and  $n_{\rm dir}$  is the number of microstructural directions of our model. Since we are unable to measure the deformation in the thickness direction of the mesh, we assume that the mesh is perfectly incompressible,  $I_3=1$ . In our biaxial extension tests, we stretch the sample in two orthogonal directions,  $\lambda_1 \geq 1$  and  $\lambda_2 \geq 1$ . The incompressibility condition,  $I_3 = \lambda_1^2 \lambda_2^2 \lambda_3^2 = 1$ , defines the stretch in the thickness direction as  $\lambda_3 = (\lambda_1 \lambda_2)^{-1} \leq 1$ . We assume that the deformation remains homogeneous and shear free,

and the deformation gradient F remains diagonal,

$$\mathbf{F} = \operatorname{diag}\left\{\lambda_1, \lambda_2, \left(\lambda_1 \lambda_2\right)^{-1}\right\}. \tag{5}$$

Next, we specify the invariants (4) in terms of the stretches  $\lambda_1$  and  $\lambda_2$  for two the microstructural architectures in Figs. 1 and 2, the two-fiber model and the three-fiber model.

### 2.3.1. Two-fiber model

For the two-fiber model, we assume that we can represent the mesh through two orthogonal fiber families, one in the warp direction  ${\bf w}$ , and one in the shute direction  ${\bf s}$ , inclined against the warp direction by  $\pi/2=90^\circ$ ,

$$\mathbf{w} = \begin{bmatrix} \cos (\alpha_w), \sin (\alpha_w), 0 \end{bmatrix}^{t}$$

$$\mathbf{s} = \begin{bmatrix} -\sin (\alpha_w), \cos (\alpha_w), 0 \end{bmatrix}^{t},$$
(6)

where  $\alpha_w$  is the warp angle, the angle of the warp direction against the 1-direction. We now specify the invariants (4) in terms of the biaxial stretches  $\lambda_1$  and  $\lambda_2$  and the warp angle  $\alpha_w$ ,

$$I_{1} = \lambda_{1}^{2} + \lambda_{2}^{2} + (\lambda_{1}\lambda_{2})^{-2}$$

$$I_{2} = \lambda_{1}^{-2} + \lambda_{2}^{-2} + (\lambda_{1}\lambda_{2})^{2}$$

$$I_{4w} = \lambda_{1}^{2}\cos^{2}(\alpha_{w}) + \lambda_{2}^{2}\sin^{2}(\alpha_{w}) = \lambda_{w}^{2}$$

$$I_{4s} = \lambda_{1}^{2}\sin^{2}(\alpha_{w}) + \lambda_{2}^{2}\cos^{2}(\alpha_{w}) = \lambda_{s}^{2}$$

$$I_{8ws} = (\lambda_{2}^{2} - \lambda_{1}^{2})\sin(\alpha_{w})\cos(\alpha_{w})$$
(7)

and take their derivatives,

$$\begin{split} &\partial_{F}I_{1} &= 2 \text{ diag } \left\{ \lambda_{1}, \ \lambda_{2}, \ \left(\lambda_{1}\lambda_{2}\right)^{-1} \right\} \\ &\partial_{F}I_{2} &= 2 \text{ diag } \left\{ \lambda_{1}\lambda_{2}^{2} + \lambda_{1}^{-1}\lambda_{2}^{-2}, \lambda_{1}^{2}\lambda_{2} + \lambda_{1}^{-2}\lambda_{2}^{-1}, \lambda_{1}\lambda_{2}^{-1} + \lambda_{1}^{-1}\lambda_{2} \right\} \\ &\partial_{F}I_{4w} &= 2 \text{ diag } \left\{ \lambda_{1}\cos^{2}(\alpha_{w}), \lambda_{2}\sin^{2}(\alpha_{w}), 0 \right\} \\ &\partial_{F}I_{4s} &= 2 \text{ diag } \left\{ \lambda_{1}\sin^{2}(\alpha_{w}), \lambda_{2}\cos^{2}(\alpha_{w}), 0 \right\} \\ &\partial_{F}I_{8ws} &= \text{ diag } \left\{ -\lambda_{1}\sin\left(2\alpha_{w}\right), \lambda_{2}\sin\left(2\alpha_{w}\right), 0 \right\}. \end{split}$$

Our two-fiber model has five distinct invariants,  $I_1$ ,  $I_2$ ,  $I_{4w}$ ,  $I_{4s}$ ,  $I_{8ws}$ , where  $I_{4w}$  and  $I_{4s}$  take the interpretation of the squared stretches in the warp and shute directions  $\lambda_w$  and  $\lambda_s$ , and  $I_{8ws}$  characterizes the interaction between the warp and shute directions. For the special case of the 0/90 orientation, the anisotropic invariants are

$$I_{4w} = \lambda_1^2$$
  $I_{4s} = \lambda_2^2$   $I_{8ws} = 0$ , (9)

and we already see that this setup is incapable of probing the interaction between the warp and shute directions since  $I_{8ws} = 0$ . For the special case of the +45/-45 orientation, the anisotropic invariants are

$$I_{4w} = \frac{1}{2} \left[ \lambda_1^2 + \lambda_2^2 \right] \quad I_{4s} = \frac{1}{2} \left[ \lambda_1^2 + \lambda_2^2 \right] \quad I_{8ws} = \frac{1}{2} \left[ -\lambda_1^2 + \lambda_2^2 \right],$$
 (10)

and we already see that this setup is incapable of distinguishing between the warp and shute directions since  $I_{4w} = I_{4s}$ .

### 2.3.2. Three-fiber model

The potential shortcomings of the two-fiber model motivate a more advanced three-fiber model with three fiber families, one in the warp direction  $\mathbf{w}$ , and two in the shute directions  $\mathbf{s}_{l}$  and  $\mathbf{s}_{ll}$ , symmetrically inclined against the warp direction by  $+\pi/3=+60^{\circ}$  and  $-\pi/3=-60^{\circ}$ ,

$$\mathbf{w} = \begin{bmatrix} \cos (\alpha_w), & \sin (\alpha_w), & 0 \end{bmatrix}^{t}$$

$$\mathbf{s}_{l} = \begin{bmatrix} \cos (\alpha_w + \frac{1}{3}\pi), \sin (\alpha_w + \frac{1}{3}\pi), & 0 \end{bmatrix}^{t}$$

$$\mathbf{s}_{ll} = \begin{bmatrix} \cos (\alpha_w - \frac{1}{3}\pi), \sin (\alpha_w - \frac{1}{3}\pi), & 0 \end{bmatrix}^{t}$$
(11)

where  $\alpha_w$  denotes the warp angle against the 1-direction. We now specify the invariants (4) in terms of the biaxial stretches  $\lambda_1$  and  $\lambda_2$  and the warp angle  $\alpha_w$ ,

$$\begin{split} I_{1} &= \lambda_{1}^{2} + \lambda_{2}^{2} + (\lambda_{1}\lambda_{2})^{-2} \\ I_{2} &= \lambda_{1}^{-2} + \lambda_{2}^{-2} + (\lambda_{1}\lambda_{2})^{2} \\ I_{4w} &= \lambda_{1}^{2} \cos^{2}(\alpha_{w}) \\ I_{4s_{l}} &= \lambda_{1}^{2} \cos^{2}(\alpha_{w}) \\ I_{4s_{l}} &= \lambda_{1}^{2} \cos^{2}(\alpha_{w} + \frac{1}{3}\pi) \\ I_{4s_{ll}} &= \lambda_{1}^{2} \cos^{2}(\alpha_{w} + \frac{1}{3}\pi) \\ I_{8w_{l}} &= \lambda_{1}^{2} \cos^{2}(\alpha_{w} - \frac{1}{3}\pi) \\ I_{8ws_{l}} &= \lambda_{1}^{2} \cos(\alpha_{w}) \cos(\alpha_{w} + \frac{1}{3}\pi) + \lambda_{2}^{2} \sin^{2}(\alpha_{w} - \frac{1}{3}\pi) \\ I_{8ws_{ll}} &= \lambda_{1}^{2} \cos(\alpha_{w}) \cos(\alpha_{w} + \frac{1}{3}\pi) + \lambda_{2}^{2} \sin(\alpha_{w}) \sin(\alpha_{w} + \frac{1}{3}\pi) \\ I_{8s_{l}s_{ll}} &= \lambda_{1}^{2} \cos(\alpha_{w}) \cos(\alpha_{w} + \frac{1}{3}\pi) \cos(\alpha_{w} - \frac{1}{3}\pi) \\ &+ \lambda_{2}^{2} \sin(\alpha_{w} + \frac{1}{3}\pi) \sin(\alpha_{w} - \frac{1}{3}\pi) \end{split}$$

$$(12)$$

Our three-fiber model has eight distinct invariants,  $I_1$ ,  $I_2$ ,  $I_{4w}$ ,  $I_{4s_I}$ ,  $I_{4s_{II}}$ ,  $I_{8ws_{II}}$ ,  $I_{8ws_{II}}$ ,  $I_{8s_Is_{II}}$ , where  $I_{4w}$ ,  $I_{4s_{II}}$ ,  $I_{4s_{II}}$  take the interpretation of the squared stretches in the warp and shute directions  $\lambda_w$ ,  $\lambda_{s_I}$ ,  $\lambda_{s_{II}}$  and  $I_{8ws_I}$ ,  $I_{8ws_{II}}$ ,  $I_{8s_Is_{II}}$  characterizes the interaction between the warp and shute directions. For the special case of the 0/+60/-60 orientation, the anisotropic invariants are

$$\begin{array}{lll} I_{4w} & = & \lambda_1^2 & I_{4s_I} & = \frac{1}{4}[\lambda_1^2 + 3\lambda_2^2] & I_{4s_{II}} & = \frac{1}{4}[\lambda_1^2 + 3\lambda_2^2] \\ I_{8ws_I} & = \frac{1}{2}\lambda_1^2 & I_{8ws_{II}} & = \frac{1}{2}\lambda_1^2 & I_{8s_Is_{II}} & = \frac{1}{4}[\lambda_1^2 - 3\lambda_2^2], \end{array} \tag{13}$$

and we notice the microstructural symmetry of the two shute directions as  $I_{4s_I} = I_{4s_{II}}$  and  $I_{8ws_I} = I_{8ws_{II}}$ . For the special case of the -45/+15/+75 orientation, the anisotropic invariants are

$$I_{4w} = \left[ +\frac{1}{2} \right] \lambda_{1}^{2} + \left[ +\frac{1}{2} \right] \lambda_{2}^{2}$$

$$I_{4s_{I}} = \left[ +\frac{1}{2} - \frac{1}{4}\sqrt{3} \right] \lambda_{1}^{2} + \left[ +\frac{1}{2} + \frac{1}{4}\sqrt{3} \right] \lambda_{2}^{2}$$

$$I_{4s_{II}} = \left[ +\frac{1}{2} + \frac{1}{4}\sqrt{3} \right] \lambda_{1}^{2} + \left[ +\frac{1}{2} - \frac{1}{4}\sqrt{3} \right] \lambda_{2}^{2}$$

$$I_{8ws_{I}} = \left[ +\frac{1}{4} - \frac{1}{4}\sqrt{3} \right] \lambda_{1}^{2} + \left[ +\frac{1}{4} + \frac{1}{4}\sqrt{3} \right] \lambda_{2}^{2}$$

$$I_{8ws_{II}} = \left[ +\frac{1}{4} + \frac{1}{4}\sqrt{3} \right] \lambda_{1}^{2} + \left[ +\frac{1}{4} - \frac{1}{4}\sqrt{3} \right] \lambda_{2}^{2}$$

$$I_{8s_{I}s_{II}} = \left[ -\frac{1}{4} \right] \lambda_{1}^{2} + \left[ -\frac{1}{4} \right] \lambda_{2}^{2},$$

$$(14)$$

and we immediately notice that the three-fiber model invariants are much richer than the two-fiber model invariants.

### 2.4. Constitutive modeling

A constitutive model is a material-specific function that estimates the stress in a material given its deformation history. In the case of a hyperelastic constitutive model, the stress, in our case the Piola stress P, only depends on the current deformation state, in our case the deformation gradient F, such that P = P(F). To satisfy thermodynamic consistency, we can express the stress as a function of the strain energy density  $\psi$  as  $P = \partial \psi(F)/\partial F$ , which we reformulate in terms of our set of invariants  $\psi(I_1, I_2, I_3, I_{4i}, I_{8ij})$ ,

$$\mathbf{P} = \frac{\partial \psi}{\partial I_1} \frac{\partial I_1}{\partial \mathbf{F}} + \frac{\partial \psi}{\partial I_2} \frac{\partial I_2}{\partial \mathbf{F}} + \frac{\partial \psi}{\partial I_3} \frac{\partial I_3}{\partial \mathbf{F}} + \frac{\partial \psi}{\partial I_{4i}} \frac{\partial I_{4i}}{\partial \mathbf{F}} + \frac{\partial \psi}{\partial I_{8ij}} \frac{\partial I_{8ij}}{\partial \mathbf{F}}.$$
 (15)

where  $i,j=1,\ldots,n_{\rm dir}$  is the number of microstructural directions of our model. We explicitly enforce incompressibility by selecting the term in the third invariant as  $\psi(I_3)=-p\ [J-1\ ]$ , such that  $\partial\psi/\partial I_3\cdot\partial I_3/\partial {\pmb F}=-p\ {\pmb F}^{-t}$ . Here p acts as a Lagrange multiplier that we determine from the zero-thickness-stress condition.

### 2.5. Biaxial testing

In biaxial extension tests, we stretch the sample in two orthogonal directions,  $\lambda_1 \geq 1$  and  $\lambda_2 \geq 1$ , and, by incompressibility,

 $\lambda_3 = (\lambda_1 \lambda_2)^{-1} \le 1$ . We assume that the deformation remains homogeneous and shear free, and that the resulting Piola stress **P** remains diagonal.

$$\mathbf{P} = \text{diag} \{ P_{11}, P_{22}, 0 \}. \tag{16}$$

We use the isotropic first and second invariants  $I_1 = \lambda_1^2 + \lambda_2^2 + (\lambda_1\lambda_2)^{-2}$  and  $I_2 = \lambda_1^{-2} + \lambda_2^{-2} + (\lambda_1\lambda_2)^2$  from Eq. (7) and their derivatives from Eq. (8) to determine the pressure p from the zero-thickness-stress condition in the third direction,

$$P_{33} = 0 \quad \text{thus} \quad p = 2\frac{1}{\lambda_1^2 \lambda_2^2} \frac{\partial \psi}{\partial I_1} + 2\left(\frac{1}{\lambda_1^2} + \frac{1}{\lambda_2^2}\right) \frac{\partial \psi}{\partial I_2}. \tag{17}$$

Eqs. (15) and (17) then provide an explicit analytical expression for the nominal stresses  $P_{11}$  and  $P_{22}$  in terms of the stretches  $\lambda_1$  and  $\lambda_2$  and the warp angle  $\alpha_w$ . We acknowledge that biaxial testing is limited to characterize the stress-stretch behavior within the plane, and does not allow us to make any assessment of the out-of-plane behavior of the fabric.

### 2.5.1. Two-fiber model

For the two-fiber model, the free energy function is a function of five terms,  $\psi = \psi(I_1, I_2, I_{4w}, I_{4s}, I_{8ws})$ , and the nominal stresses  $P_{11}$  and  $P_{22}$  have five terms, one for each invariant,

$$P_{11} = 2\left(\lambda_{1} - \frac{1}{\lambda_{1}^{3}\lambda_{2}^{2}}\right) \frac{\partial \psi}{\partial I_{1}} + 2\left(\lambda_{1}\lambda_{2}^{2} - \frac{1}{\lambda_{1}^{3}}\right) \frac{\partial \psi}{\partial I_{2}}$$

$$+2\lambda_{1}\cos^{2}(\alpha_{w}) \frac{\partial \psi}{\partial I_{4w}} + 2\lambda_{1}\sin^{2}(\alpha_{w}) \frac{\partial \psi}{\partial I_{4s}}$$

$$-\lambda_{1}\sin(2\alpha_{w}) \frac{\partial \psi}{\partial I_{8ws}}$$

$$P_{22} = 2\left(\lambda_{2} - \frac{1}{\lambda_{1}^{2}\lambda_{2}^{3}}\right) \frac{\partial \psi}{\partial I_{1}} + 2\left(\lambda_{1}^{2}\lambda_{2} - \frac{1}{\lambda_{2}^{3}}\right) \frac{\partial \psi}{\partial I_{2}}$$

$$+2\lambda_{2}\sin^{2}(\alpha_{w}) \frac{\partial \psi}{\partial I_{4w}} + 2\lambda_{2}\cos^{2}(\alpha_{w}) \frac{\partial \psi}{\partial I_{4s}}$$

$$+\lambda_{2}\sin(2\alpha_{w}) \frac{\partial \psi}{\partial I_{8ws}}.$$
(18)

Here we make an important observation: Counterintuitively, the eighth-invariant term,  $\partial \psi/\partial I_{8ws}$ , contributes negatively to the stresses in the 1-direction and positively to the stresses in the 2-direction. This contradicts our general intuition, and potentially violates the condition of material symmetry. We therefore drop the dependence on the eighth invariant and reduce our set of invariants to four,  $\psi=\psi(I_1,I_2,I_{4w},I_{4s})$ . For the special case of the 0/90 orientation, with  $\alpha_w=0$   $\pi=0^\circ$ , the biaxial Piola stresses simplify to

$$P_{11} = 2\left(\lambda_{1} - \frac{1}{\lambda_{1}^{3}\lambda_{2}^{2}}\right) \frac{\partial \psi}{\partial I_{1}} + 2\left(\lambda_{1}\lambda_{2}^{2} - \frac{1}{\lambda_{1}^{3}}\right) \frac{\partial \psi}{\partial I_{2}} + 2\lambda_{1} \frac{\partial \psi}{\partial I_{4w}}$$

$$P_{22} = 2\left(\lambda_{2} - \frac{1}{\lambda_{1}^{2}\lambda_{2}^{3}}\right) \frac{\partial \psi}{\partial I_{1}} + 2\left(\lambda_{1}^{2}\lambda_{2} - \frac{1}{\lambda_{2}^{3}}\right) \frac{\partial \psi}{\partial I_{2}} + 2\lambda_{2} \frac{\partial \psi}{\partial I_{4s}}.$$

$$(19)$$

For the special case of the -45/+45 orientation, with  $\alpha_w = -\pi/4 = -45^\circ$ , the stresses are

$$P_{11} = 2\left(\lambda_{1} - \frac{1}{\lambda_{1}^{3}\lambda_{2}^{2}}\right) \frac{\partial \psi}{\partial I_{1}} + 2\left(\lambda_{1}\lambda_{2}^{2} - \frac{1}{\lambda_{1}^{3}}\right) \frac{\partial \psi}{\partial I_{2}} + \lambda_{1}\left(\frac{\partial \psi}{\partial I_{4w}} + \frac{\partial \psi}{\partial I_{4s}}\right)$$

$$P_{22} = 2\left(\lambda_{2} - \frac{1}{\lambda_{1}^{2}\lambda_{2}^{3}}\right) \frac{\partial \psi}{\partial I_{1}} + 2\left(\lambda_{1}^{2}\lambda_{2} - \frac{1}{\lambda_{2}^{3}}\right) \frac{\partial \psi}{\partial I_{2}} + \lambda_{2}\left(\frac{\partial \psi}{\partial I_{4w}} + \frac{\partial \psi}{\partial I_{4s}}\right).$$

$$(20)$$

### 2.5.2. Three-fiber model

For the three-fiber model, for similar reasons as above, we drop the dependence on the eighth invariants and reduce our set of invariants to five,  $\psi=\psi(I_1,I_2,I_{4w},I_{4s_I},I_{4s_{II}})$ . We now express the fourth invariants of the three-fiber model,  $I_{4w}$ ,  $I_{4s_I}$ ,  $I_{4s_{II}}$ , in terms of the invariants of the two-fiber model,  $I_{4w}$ ,  $I_{4s}$ ,  $I_{8ws}$ ,  $I_{4(\circ)}=I_{4w}\cos^2(\alpha_\circ)+I_s\sin^2(\alpha_\circ)+I_{8ws}\sin(2\alpha_\circ)$ . For our specific three-fiber model, with  $(\circ)=\{w,s_I,s_{II}\}$ , and  $\alpha_\circ=\{0,+\frac{1}{3}\pi,-\frac{1}{3}\pi\}$ , this allows us express the nominal stresses  $P_{11}$  and  $P_{22}$  using Eq. (18),

$$\begin{split} P_{11} &= 2 \left( \lambda_{1} - \frac{1}{\lambda_{1}^{3} \lambda_{2}^{2}} \right) \frac{\partial \psi}{\partial I_{1}} + 2 \left( \lambda_{1} \lambda_{2}^{2} - \frac{1}{\lambda_{1}^{3}} \right) \frac{\partial \psi}{\partial I_{2}} \\ &+ 2 \lambda_{1} cos^{2} (\alpha_{w}) \left( \frac{\partial \psi}{\partial I_{4w}} + \frac{1}{4} \frac{\partial \psi}{\partial I_{4s_{I}}} + \frac{1}{4} \frac{\partial \psi}{\partial I_{4s_{II}}} \right) \\ &+ 2 \lambda_{1} sin^{2} (\alpha_{w}) \left( \frac{3}{4} \frac{\partial \psi}{\partial I_{4s_{I}}} + \frac{3}{4} \frac{\partial \psi}{\partial I_{4s_{II}}} \right) \\ &- \lambda_{1} sin(2\alpha_{w}) \left( \frac{\sqrt{3}}{2} \frac{\partial \psi}{\partial I_{4s_{I}}} - \frac{\sqrt{3}}{2} \frac{\partial \psi}{\partial I_{4s_{II}}} \right) \\ P_{22} &= 2 \left( \lambda_{2} - \frac{1}{\lambda_{1}^{2} \lambda_{2}^{3}} \right) \frac{\partial \psi}{\partial I_{1}} + 2 \left( \lambda_{1}^{2} \lambda_{2} - \frac{1}{\lambda_{2}^{3}} \right) \frac{\partial \psi}{\partial I_{2}} \\ &+ 2 \lambda_{2} cos^{2} (\alpha_{w}) \left( \frac{\partial \psi}{\partial I_{4w}} + \frac{1}{4} \frac{\partial \psi}{\partial I_{4s_{I}}} + \frac{1}{4} \frac{\partial \psi}{\partial I_{4s_{II}}} \right) \\ &+ 2 \lambda_{2} sin^{2} (\alpha_{w}) \left( \frac{3}{4} \frac{\partial \psi}{\partial I_{4s_{I}}} + \frac{3}{4} \frac{\partial \psi}{\partial I_{4s_{II}}} \right) \\ &- \lambda_{2} sin(2\alpha_{w}) \left( \frac{\sqrt{3}}{2} \frac{\partial \psi}{\partial I_{4s_{I}}} - \frac{\sqrt{3}}{2} \frac{\partial \psi}{\partial I_{4s_{II}}} \right). \end{split}$$

For the special case of the 0/+60/-60 orientation, with  $\alpha_w = 0 \pi = 0^\circ$ , the biaxial Piola stresses become

$$P_{11} = 2\left(\lambda_{1} - \frac{1}{\lambda_{1}^{3}\lambda_{2}^{2}}\right) \frac{\partial \psi}{\partial I_{1}} + 2\left(\lambda_{1}\lambda_{2}^{2} - \frac{1}{\lambda_{1}^{3}}\right) \frac{\partial \psi}{\partial I_{2}}$$

$$+ \frac{1}{2}\lambda_{1}\left(4\frac{\partial \psi}{\partial I_{4w}} + \frac{\partial \psi}{\partial I_{4s_{I}}} + \frac{\partial \psi}{\partial I_{4s_{II}}}\right)$$

$$P_{22} = 2\left(\lambda_{2} - \frac{1}{\lambda_{1}^{2}\lambda_{2}^{2}}\right) \frac{\partial \psi}{\partial I_{1}} + 2\left(\lambda_{1}^{2}\lambda_{2} - \frac{1}{\lambda_{2}^{3}}\right) \frac{\partial \psi}{\partial I_{2}}$$

$$+ \frac{3}{2}\lambda_{1}\left(\frac{\partial \psi}{\partial I_{4s_{I}}} + \frac{\partial \psi}{\partial I_{4s_{II}}}\right).$$
(22)

For the special case of the -45/+15/+75 orientation, with  $\alpha_w=-\pi/4=-45^\circ$ , the biaxial Piola stresses are

$$\begin{split} P_{11} &= 2 \left( \lambda_1 - \frac{1}{\lambda_1^3 \lambda_2^2} \right) \frac{\partial \psi}{\partial I_1} + 2 \left( \lambda_1 \lambda_2^2 - \frac{1}{\lambda_1^3} \right) \frac{\partial \psi}{\partial I_2} \\ &+ \lambda_1 \left( \frac{\partial \psi}{\partial I_{4w}} + \left( 1 + \frac{\sqrt{3}}{2} \right) \frac{\partial \psi}{\partial I_{4s_I}} + \left( 1 - \frac{\sqrt{3}}{2} \right) \frac{\partial \psi}{\partial I_{4s_I}} \right) \\ P_{22} &= 2 \left( \lambda_2 - \frac{1}{\lambda_1^2 \lambda_2^3} \right) \frac{\partial \psi}{\partial I_1} + 2 \left( \lambda_1^2 \lambda_2 - \frac{1}{\lambda_2^3} \right) \frac{\partial \psi}{\partial I_2} \\ &+ \lambda_2 \left( \frac{\partial \psi}{\partial I_{4w}} + \left( 1 - \frac{\sqrt{3}}{2} \right) \frac{\partial \psi}{\partial I_{4s_I}} + \left( 1 + \frac{\sqrt{3}}{2} \right) \frac{\partial \psi}{\partial I_{4s_I}} \right). \end{split}$$

### 2.6. Constitutive neural networks

Motivated by the previous considerations, we design two constitutive neural networks to learn the free energy function  $\psi$ , a two-fiber network based on four invariants and a three-fiber network based on five invariants.

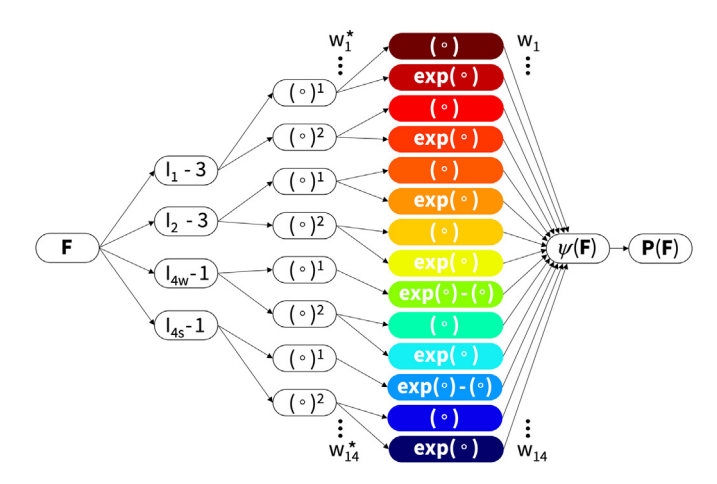


**Fig. 3.** Two-fiber constitutive neural network. The network takes the two isotropic invariants  $I_1$  and  $I_2$  and the two anisotropic invariants  $I_{4w}$  and  $I_{4s}$  of the warp and shute directions  $\vec{w}$  and  $\vec{s}$  as input. The first layer generates powers  $(\circ)$  and  $(\circ)^2$  of the input and the second layer applies the identity  $(\circ)$  and exponential function  $(\exp(\circ))$  to these powers. The network learns the free energy function  $\psi$  as the weighted sum of the final layer, from which it derives the stress P.

### 2.6.1. Two-fiber network

Our first neural network approximates a strain energy function in terms of four invariants  $I_1$ ,  $I_2$ ,  $I_{4w}$ ,  $I_{4s}$  and has 28 parameters or network weights,  $\vec{w} = \{w_1, \dots, w_{14}; w_1^*, \dots, w_{14}^*\}$ , 14 internal weights  $w_i^*$  between its two hidden layers and 14 external weights  $w_i$  out of its final hidden layer. We assume that the individual contributions to the free energy are fully decoupled. For the isotropic terms  $\psi(I_1)$  and  $\psi(I_2)$ , we adapt an isotropic constitutive neural network initially designed for rubber-like materials [26]. For the anisotropic terms  $\psi(I_{4w})$  and  $\psi(I_{4s})$ , we adapt an anisotropic constitutive neural network initially designed for arteries [45], with the additional constraint that the linear and exponential linear terms in the warp direction,  $-w_9w_9^*[I_{4w}-1]$  and  $w_9[\exp(w_9^*[I_4-1])-1]$ , and in the shute direction,  $-w_{12}w_{12}^*[I_{4s}-1]$ 1] and  $w_{12}[\exp(w_{12}^*[I_4-1])-1]$ , are not independent but share the same weights [63]. The free energy function for the two-fiber network takes the following explicit form,

$$\psi = w_1 \ w_1^* \ [I_1 \ -3] + w_2 \ [\exp(w_2^* \ [I_1 \ -3] \ ) - 1]$$

$$+ w_3 \ w_3^* \ [I_1 \ -3]^2 + w_4 \ [\exp(w_4^* \ [I_1 \ -3]^2) - 1]$$

$$+ w_5 \ w_5^* \ [I_2 \ -3] + w_6 \ [\exp(w_6^* \ [I_2 \ -3] \ ) - 1]$$

$$+ w_7 \ w_7^* \ [I_2 \ -3]^2 + w_8 \ [\exp(w_8^* \ [I_2 \ -3]^2) - 1]$$

$$- w_9 \ w_9^* \ [I_{4w} - 1] + w_9 \ [\exp(w_9^* \ [I_{4w} - 1] \ ) - 1]$$

$$+ w_{10} \ w_{10}^* \ [I_{4w} - 1]^2 + w_{11} \ [\exp(w_{11}^* \ [I_{4w} - 1]^2) - 1]$$

$$- w_{12} \ w_{12}^* \ [I_{4s} \ -1] + w_{12} \ [\exp(w_{12}^* \ [I_{4s} \ -1] \ ) - 1]$$

$$+ w_{13} \ w_{13}^* \ [I_{4s} \ -1]^2 + w_{14} \ [\exp(w_{14}^* \ [I_{4s} \ -1]^2) - 1] .$$

Fig. 3 summarizes the architecture of the two-fiber family constitutive neural network.

### 2.6.2. Three-fiber architecture

Our second model architecture approximates a strain energy function in terms of five invariants  $I_1$ ,  $I_2$ ,  $I_{4w}$ ,  $I_{4sI}$ ,  $I_{4sII}$  and has 28 parameters or network weights,  $\vec{w} = \{w_1, \ldots, w_{14}; w_1^*, \ldots, w_{14}^*\}$ , 14 internal weights  $w_i^*$  between its two hidden layers and 14 external weights  $w_i$  out of its final hidden layer. We use a similar neural network as before, and assume that the two shute directions  $\vec{s_I}$  and  $s_{II}$  have the same microstructure and share the same weights  $w_{12}$ ,  $w_{13}$ ,  $w_{14}$  and  $w_{12}^*$ ,  $w_{13}^*$ ,  $w_{14}^*$ . The free energy function for the

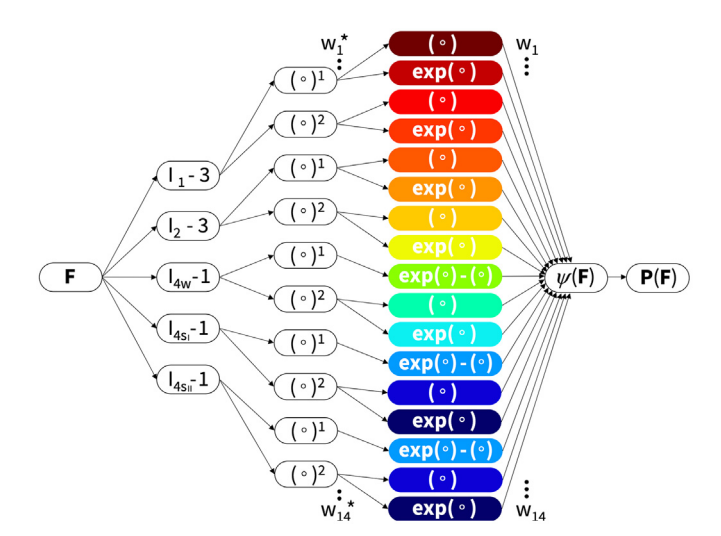


**Fig. 4.** Three-fiber constitutive neural network. The network takes the two isotropic invariants  $I_1$  and  $I_2$  and the three anisotropic invariants  $I_{4w}$  and  $I_{4s_I}$  and  $I_{4s_I}$  of the warp and shute directions  $\vec{w}$  and  $\vec{s_I}$  and  $\vec{s_I}$  as input. The first layer generates powers  $(\circ)$  and  $(\circ)^2$  of the input and the second layer applies the identity  $(\circ)$  and exponential function  $(\exp(\circ))$  to these powers. The network learns the free energy function  $\psi$  as the weighted sum of the final layer, from which it derives the stress  $\vec{P}$ . We assume that the two shute directions  $\vec{s_I}$  and  $s_{II}$  have the same microstructure and share the same weights.

three-fiber network takes the following explicit form,

$$\psi = w_{1} \ w_{1}^{*} \ [I_{1} \ -3] + w_{2} \ [\exp(w_{2}^{*} \ [I_{1} \ -3]) - 1]$$

$$+ w_{3} \ w_{3}^{*} \ [I_{1} \ -3]^{2} + w_{4} \ [\exp(w_{4}^{*} \ [I_{1} \ -3]^{2}) - 1]$$

$$+ w_{5} \ w_{5}^{*} \ [I_{2} \ -3] + w_{6} \ [\exp(w_{6}^{*} \ [I_{2} \ -3]) - 1]$$

$$+ w_{7} \ w_{7}^{*} \ [I_{2} \ -3]^{2} + w_{8} \ [\exp(w_{6}^{*} \ [I_{2} \ -3]^{2}) - 1]$$

$$- w_{9} \ w_{9}^{*} \ [I_{4w} \ -1] + w_{9} \ [\exp(w_{9}^{*} \ [I_{4w} \ -1]) - 1]$$

$$+ w_{10} \ w_{10}^{*} \ [I_{4w} \ -1]^{2} + w_{11} \ [\exp(w_{11}^{*} \ [I_{4w} \ -1]^{2}) - 1]$$

$$- w_{12} \ w_{12}^{*} \ [I_{4s_{1}} \ -1] + w_{12} \ [\exp(w_{11}^{*} \ [I_{4s_{1}} \ -1]) - 1]$$

$$+ w_{13} \ w_{13}^{*} \ [I_{4s_{1}} \ -1] + w_{12} \ [\exp(w_{12}^{*} \ [I_{4s_{1}} \ -1]) - 1]$$

$$+ w_{13} \ w_{13}^{*} \ [I_{4s_{1}} \ -1]^{2} + w_{14} \ [\exp(w_{14}^{*} \ [I_{4s_{1}} \ -1])^{2}) - 1] .$$

$$(25)$$

Fig. 4 summarizes the architecture of the three-fiber family constitutive neural network.

#### 2.7. Model training

To discover models and parameters  $\vec{w} = \{w_1, \dots, w_{14}; w_1^*, \dots, w_{14}^*\}$  that best describe our synthetic mesh, we use the Adam optimizer to perform gradient descent on a weighted least squared error loss function L that penalizes the error between the discovered model  $P(F_i, \vec{w})$  and the experimental data  $\hat{P}_i$  at  $i = 1, \dots, n_{\text{data}}$  discrete points, supplemented by  $L_p$  regularization,

$$L(\vec{w}; \mathbf{F}) = \frac{1}{n_{\text{data}}} \sum_{i=1}^{n_{\text{data}}} \left| \left| \frac{\mathbf{P}(\mathbf{F}_i, \vec{w}) - \hat{\mathbf{P}}_i}{P_{\text{max}}} \right| \right|^2 + L_p(\vec{w}) \rightarrow \min_{\mathbf{w}}.$$
 (26)

To account for all experiments equally, we weigh the error of each of the stress-stretch curve by the inverse of its maximum stress  $P_{\max}$  [32]. For the  $L_0$  regularization, we supplement the loss function by an  $\alpha$ -weighted regularization term,  $L_0=\alpha \mid \mid \vec{w} \mid \mid_0$  with  $\mid \mid \vec{w} \mid \mid_0 = \sum_{i=1}^{n_w} I(w_i \neq 0)$ , where  $I(\circ)$  is the indicator function that is one if the condition inside the parenthesis is true and zero otherwise. In practice, instead of solving the full discrete combinatorial problem and exploring all possible  $2^{14}=16,384$  combinations of terms, we only explore the weights and losses of the possible 14 one-term models and 91 two-term models by explicitly setting all other terms to zero. For the  $L_{0.5}$  regularization, we supplement

the loss function by an  $\alpha$ -weighted regularization,  $L_{0.5} = \alpha \mid \mid \vec{w} \mid \mid_{0.5}^{0.5}$  with  $\mid \mid \vec{w} \mid \mid_{0.5}^{0.5} = \sum_{i=1}^{14} \sqrt{\mid P_i(w_i, w_i^*) \mid}$ , where  $P_i$  is the color-coded area of the stress contribution of the i-th term across all loading modes that we compute by summing the strain energies at the maximum displacement for each loading mode. The penalty parameter  $\alpha$  sets the strength of the  $L_{0.5}$  regularization. We increase  $\alpha$  progressively until the fit of the model to the data starts to become noticeably worse. To minimize the training time and ensure that the initial model creates predictions that are of the same order of magnitude as the data, we initialize all weights with a uniform distribution  $\vec{w} = \sim \text{Uniform}([0, \gamma))$ , where we choose  $\gamma$  such that, in expectation, the total area under the measured stress-stretch curve equals the total area under the predicted stress-stretch curve.

### 3. Results

We perform all experiments as described in Section 2.1 and examine the data for each individual experiment. Figs. 5 and 6 show the loading and unloading curves for the 0/90 orientation in the top two rows and for the -45/+45 orientation in the bottom row. The solid lines represent the means of n=5 tests and the shaded areas represent the standard deviations. In all experiments, we observe significant hysteresis between the loading and unloading curves. The stress remains constant during the thirty-second holding between each experiment, from which we conclude that the difference in loading and unloading is a result of microstructural rearrangements of the mesh, rather than a viscous effect. For model discovery, for each experiment type, we extract the stretches and average stresses across the n=5 tests during loading and unloading and summarize the stretch-stress data of all ten experiments in Table 2.

### 3.1. Mechanical signature of warp knitted fabric

All fifteen stress-stretch curves in Figs. 5 and 6 display a similar trend: During the first half of the loading interval, the mesh behaves very compliant and the recorded stresses remain low; during the second half, the mesh stiffens and the stresses increase exponentially. Although present during both loading and unloading, this trend is less visible in the loading curves in Fig. 5 than in the unloading curves in Fig. 6, which also display smaller standard deviations. Intuitively, we expect the mesh to be stiffer in the warp than in the shute direction and Figs. 5 and 6 and Table 2 confirm our expectation: In the strip-w and strip-s tests, the peak warp stress of 484 kPa is about twice as large as the peak shute stress of 256 kPa. In the equibiaxial test, the peak warp stress of 966 kPa is about one third larger than the peak shute stress of 714 kPa. We also expect the mesh to be stiffer in the 0/90 orientation, for which the loading axes are aligned with the warp and shute directions, than in the -45/+45 orientation, for which the loading axes are rotated by 45 degrees against the warp and shute directions. In the strip-x and strip-y tests, the peak stress of 219 kPa is significantly lower than either of the two peak stresses of 484 kPa and 256 kPa of the unrotated setting. In the equibiaxial test, the peak stress of 442 kPa is also lower than two biaxial peak stresses of 966 kPa and 714 kPa of the unrotated setting. Taken together, our measurements confirm that knitted meshes display unique mechanical properties including an remarkable initial flexibility, a pronounced nonlinear stiffening, and an extreme anisotropy. To gain further insights into these characteristics, we now analyze the data using our constitutive neural networks and discover the two- and three-fiber models that best characterize our mesh.

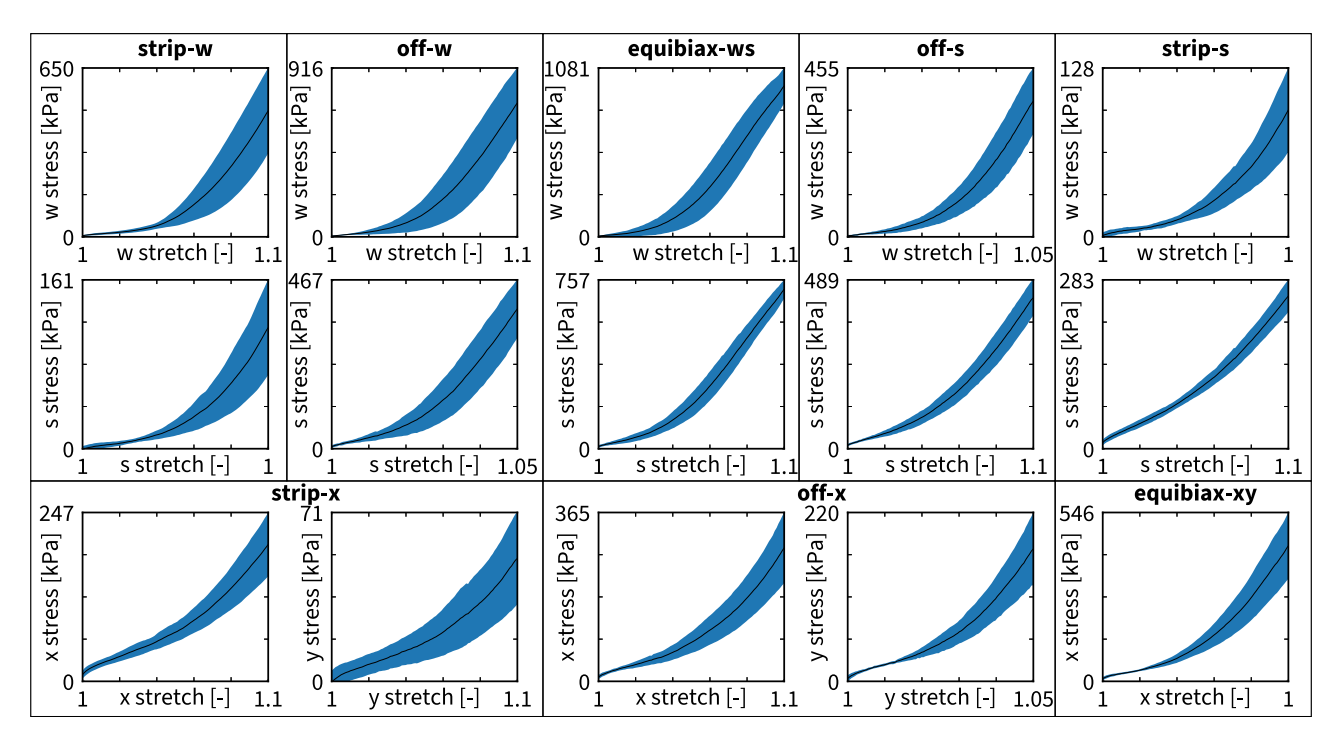


**Fig. 5.** Biaxial test data during loading. Warp and shute stress-stretch data for strip-x, off-x, equibiax, off-y, and strip-y tests in the 0/90 orientation, top rows, and in the -45/+45 orientation, bottom row. Solid lines represent the means of n = 5 tests, shaded areas represent the standard deviations.

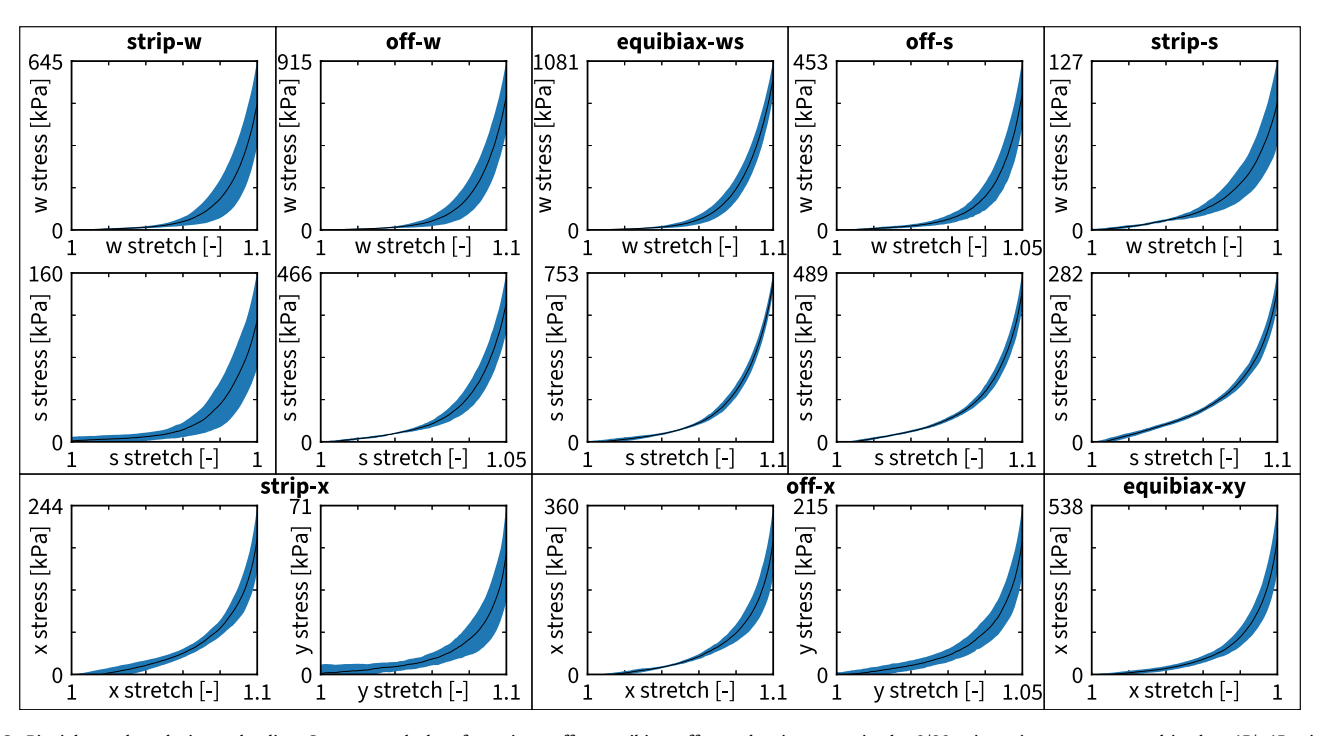


**Fig. 6.** Biaxial test data during unloading. Stress-stretch data for strip-x, off-x, equibiax, off-y, and strip-y tests in the 0/90 orientation, top rows, and in the -45/+45 orientation, bottom row. Solid lines represent the means of n = 5 tests, shaded areas represent the standard deviations.

### 3.2. Two-fiber architecture

First, we train the full network using the two-fiber architecture in Fig. 3. We initialize the model parameters randomly and train the network without any regularization. Then, we use these trained parameters to re-initialize the parameters and train the network using  $L_{0.5}$  regularization with a regularization parameter  $\alpha=0.001$ . We use data from all experiments for training. Fig. 7 shows the discovered model, with the contributions of each dis-

covered stress term in a different color. The network discovers four non-zero terms, one is the exponential linear first invariant  $I_1$  Demiray term [8], one is a quadratic first invariant  $I_1$  term, and two are the exponential quadratic fourth warp and shute invariant  $I_{4w}$  and  $I_{4s}$  Holzapfel terms [16],

$$\psi = \frac{1}{2}a_1[\exp(b_1[I_1 - 3]) - 1]/b_1 + \frac{1}{2}\mu_1[I_1 - 3]^2 + \frac{1}{2}a_2[\exp(b_2[I_{4w} - 1]^2) - 1]/b_2 + \frac{1}{2}a_3[\exp(b_3[I_{4s} - 1]^2) - 1]/b_3$$

**Table 2**Biaxial test data. Stress-stretch data for strip-x, off-x, equibiax, off-y, and strip-y tests in the 0/90 orientation, top, and in the -45/+45 orientation, bottom. Stress values are the means of n = 5 loading and unloading tests.

0/90 01	rientation		0/90 or	ientation		0/90 or	ientation		0/90 or	ientation		0/90 or	ientation	
strip-w $\lambda_w: \lambda_s = 1.10: 1.00$		off-w $\lambda_w: \lambda_s = 1.10: 1.05$		equi-biax			off-s $\lambda_w: \lambda_s = 1.05: 1.10$			strip-s $\lambda_w: \lambda_s = 1.00: 1.10$				
				$\lambda_w:\lambda_s=1.10:1.10$										
λ <sub>w</sub> [-]	$\sigma_w$ [kPa]	$\sigma_{ m s}$ [kPa]	λ <sub>w</sub> [-]	$\sigma_w$ [kPa]	$\sigma_{ m s}$ [kPa]	λ <sub>w</sub> [-]	$\sigma_w$ [kPa]	$\sigma_{ m s}$ [kPa]	λ <sub>s</sub> [-]	$\sigma_w$ [kPa]	$\sigma_{ m s}$ [kPa]	$\lambda_s$ [-]	$\sigma_w$ [kPa]	σ <sub>s</sub> [kPa]
1.000	0.00	0.00	1.000	0.00	0.00	1.000	0.00	0.00	1.000	0.00	0.00	1.000	0.00	0.00
1.006	4.49	1.59	1.006	4.88	6.88	1.006	5.68	10.01	1.006	2.82	8.59	1.006	1.76	10.0
1.013	7.12	2.70	1.013	8.82	11.91	1.013	10.11	18.32	1.013	5.41	16.36	1.013	3.00	17.2
1.019	9.68	3.54	1.019	13.66	17.67	1.019	16.06	27.79	1.019	8.16	24.28	1.019	3.94	24.3
1.025	12.93	4.72	1.025	19.45	23.20	1.025	24.63	38.59	1.025	11.59	33.14	1.025	5.11	31.4
1.031	17.01	6.14	1.031	27.21	30.27	1.031	36.91	53.24	1.031	16.10	43.14	1.031	6.77	39.3
1.038	22.62	7.97	1.038	38.38	39.25	1.038	55.25	71.20	1.038	21.61	54.36	1.038	8.79	47.7
1.044	31.55	10.21	1.044	53.89	50.07	1.044	80.88	94.46	1.044	28.99	67.80	1.044	11.37	57.0
1.050	44.58	13.31	1.050	74.58	62.77	1.050	114.03	122.29	1.050	38.82	84.24	1.050	14.41	67.3
1.056	62.93	17.64	1.056	103.79	79.64	1.056	157.77	156.84	1.056	52.57	103.39	1.056	18.01	78.8
1.063	86.50	23.21	1.063	140.76	99.45	1.063	213.88	198.11	1.063	69.17	126.07	1.063	23.21	91.8
1.069	116.72	29.97	1.069	187.30	124.63	1.069	283.90	247.19	1.069	90.47	153.03	1.069	29.22	107.
1.075	155.29	39.31	1.075	247.71	156.25	1.075	370.58	306.65	1.075	119.61	185.94	1.075	36.77	124.
1.081	204.50	51.40	1.081	322.51	193.98	1.081	473.17	374.49	1.081	155.46	225.04	1.081	45.75	145.
1.088	269.71	67.25	1.088	421.10	240.98	1.088	598.90	456.81	1.088	203.65	275.28	1.088	57.79	171.
1.094	357.00	87.38	1.094	548.29	301.55	1.094	753.88	561.17	1.094	270.62	340.53	1.094	74.18	204.
1.100	484.04	115.51	1.100	724.81	385.76	1.100	966.14	714.12	1.100	365.55	437.14	1.100	96.21	256.
				45		45				45 .		AFI	. 45	
-45	+45 orien	tation	-45/	+45 orient	tation	-45/	+45 orient	tation	-45/	+45 orien	tation	-45/-	+45 orier	itation
-45	+45 orien strip-x	tation	-45/	+45 orient	tation	-45/	+45 orien equi-biax		-45/	+45 orient	tation	-45/-	+45 orier strip-y	itation
	strip-x			off-x			equi-biax			off-y			strip-y	
$\lambda_x$ :	$strip-x$ $\lambda_y = 1.10$ $\sigma_x$	: 1.00 $\sigma_y$	$\lambda_x$ : $\lambda_x$ [-] 1.000	off-x $\lambda_y = 1.10:$ $\sigma_x$	: 1.05 $\sigma_y$	$\lambda_x$ :	equi-biax $\lambda_y = 1.10$ $\sigma_x$	: 1.10 $\sigma_y$	$\lambda_x$ :	off-y $\lambda_y = 1.05$ $\sigma_x$	: 1.10 $\sigma_y$	$\lambda_x$ :	$\frac{\text{strip-y}}{\lambda_y = 1.00}$ $\frac{\sigma_x}{\sigma_x}$	: 1.05 σ <sub>y</sub>
$\lambda_x$ : $\lambda_x$ $[-]$ 1.000	strip-x $ \lambda_y = 1.10 $ $ \sigma_x $ [kPa]	: 1.00	$\lambda_x$ :	off-x $\lambda_y = 1.10:$ $\sigma_x$ [kPa]	: 1.05	λ <sub>x</sub> :	equi-biax $\lambda_y = 1.10$ $\sigma_x$ [kPa]	: 1.10	$\lambda_x$ :	off-y $\lambda_y = 1.05$ $\sigma_x$ [kPa]	: 1.10	$\lambda_x$ : $\lambda_y$ [-]	$strip-y$ $\lambda_y = 1.00$ $\sigma_x$ [kPa]	: 1.05 $\sigma_y$ [kPa 0.00
$\lambda_x$ : $\lambda_x$ [-] 1.000 1.006 1.013	strip-x $ \frac{\lambda_y = 1.10}{\sigma_x} $ [kPa] $ 0.00 $	: 1.00 $\sigma_y$ [kPa] 0.00	$\lambda_x$ : $\lambda_x$ [-] 1.000	off-x $\lambda_y = 1.10$ $\sigma_x$ [kPa] $0.00$	1.05 σ <sub>y</sub> [kPa] 0.00	λ <sub>x</sub> : λ <sub>z</sub> [-] 1.000	equi-biax $\lambda_y = 1.10$ $\sigma_x$ [kPa] $0.00$	1.10 σ <sub>y</sub> [kPa] 0.00	λ <sub>x</sub> : λ <sub>y</sub> [-] 1.000	off-y $\lambda_y = 1.05$ $\sigma_x$ [kPa] $0.00$	: 1.10 $\sigma_y$ [kPa]  0.00	$\lambda_x$ : $\lambda_y$ [-] 1.000	$strip-y$ $\lambda_y = 1.00$ $\sigma_x$ [kPa] $0.00$	σ <sub>y</sub> [kPa 0.00 9.70 15.5
$\lambda_x$ : $\lambda_x$ [-] 1.000 1.006 1.013	strip-x $ \begin{array}{l} \lambda_y = 1.10 \\ \sigma_x \\ \text{[kPa]} \\ 0.00 \\ 9.70 \end{array} $	1.00 σ <sub>y</sub> [kPa] 0.00 2.08	$\lambda_{x}$ : $\lambda_{x}$ [-] 1.000 1.006	off-x $\lambda_y = 1.10:$ $\sigma_x$ [kPa] $0.00$ 8.78	1.05 $\sigma_y$ [kPa] 0.00 6.80	$\lambda_{x}$ : $\lambda_{x}$ [-] 1.000 1.006	equi-biax $\lambda_y = 1.10$ $\sigma_x$ [kPa] $0.00$ $9.96$	1.10 σ <sub>y</sub> [kPa] 0.00 9.96	λ <sub>x</sub> : λ <sub>y</sub> [-] 1.000 1.006	off-y $\lambda_y = 1.05$ $\sigma_x$ [kPa] $0.00$ $6.80$	: 1.10 $\sigma_y$ [kPa]  0.00 8.78	$\lambda_x$ : $\lambda_y$ [-] 1.000 1.006	$strip-y$ $\lambda_y = 1.00$ $\sigma_x$ [kPa] $0.00$ $2.08$	: 1.05 $\sigma_y$ [kPa 0.00 9.70
$\lambda_x$ : $\lambda_x$ [-]  1.000  1.006  1.013  1.019  1.025	strip-x $ \begin{array}{c} \lambda_y = 1.10 \\ \sigma_x \\ [kPa] \\ 0.00 \\ 9.70 \\ 15.58 \end{array} $	: 1.00 $\sigma_y$ [kPa]  0.00 2.08 3.36	λ <sub>x</sub> :  λ <sub>x</sub> [-]  1.000 1.006 1.013	$off-x$ $\lambda_y = 1.10$ $\sigma_x$ [kPa] $0.00$ 8.78 $14.45$	1.05 σ <sub>y</sub> [kPa] 0.00 6.80 10.71	$\lambda_x$ : $\lambda_x$ [-]  1.000  1.006  1.013	equi-biax $\lambda_y = 1.10$ $\sigma_x$ [kPa] $0.00$ $9.96$ $15.61$	.: 1.10 σ <sub>y</sub> [kPa] 0.00 9.96 15.61	λ <sub>x</sub> : λ <sub>y</sub> [-] 1.000 1.006 1.013	$off-y$ $\lambda_y = 1.05$ $\sigma_x$ [kPa] $0.00$ $6.80$ $10.71$	: 1.10 $\sigma_y$ [kPa]  0.00  8.78  14.45	$\lambda_x$ : $\lambda_y$ [-] 1.000 1.006 1.013	strip-y $ \lambda_y = 1.00 $ $ \sigma_x $ [kPa] $ 0.00 $ $ 2.08 $ $ 3.36 $	σ <sub>y</sub> [kPa 0.00 9.70 15.5 20.8 26.4
$\lambda_x$ : $\lambda_x$ [-]  1.000 1.006 1.013 1.019 1.025 1.031	strip-x $ \frac{\sigma_x}{[kPa]} $ 0.00 9.70 15.58 20.89 26.47 32.24	.: 1.00 $\sigma_y$ [kPa] 0.00 2.08 3.36 4.33 5.26 6.31	$\lambda_x$ : $\lambda_x$ [-]  1.000  1.006  1.013  1.019  1.025  1.031	$\begin{aligned} & \text{off-x} \\ & \lambda_y = 1.10 \\ & \sigma_x \\ & \text{[kPa]} \\ & 0.00 \\ & 8.78 \\ & 14.45 \\ & 19.82 \\ & 25.66 \\ & 31.86 \end{aligned}$	1.05 $\sigma_y$ [kPa] 0.00 6.80 10.71 14.15 17.83 21.74	$\lambda_x$ : $\lambda_x$ [-]  1.000  1.006  1.013  1.019	equi-biax $\lambda_{y} = 1.10$ $\sigma_{x}$ [kPa] 0.00 9.96 15.61 21.62	σ <sub>y</sub> [kPa] 0.00 9.96 15.61 21.62	$\lambda_x$ : $\lambda_y$ [-]  1.000  1.006  1.013  1.019  1.025  1.031	off-y $\lambda_{y} = 1.05$ $\sigma_{x}$ [kPa] 0.00 6.80 10.71 14.15	: 1.10 $\sigma_y$ [kPa]  0.00 8.78 14.45 19.82	$\lambda_x$ : $\lambda_y$ [-]  1.000 1.006 1.013 1.019 1.025 1.031	strip-y $ \frac{\lambda_{y} = 1.00}{\sigma_{x}} $ [kPa] $ 0.00 2.08 3.36 4.33$	σ <sub>y</sub> [kPa 0.00 9.70 15.5 20.8 26.4 32.2
λ <sub>x</sub> :	strip-x $ \begin{array}{c} \sigma_x \\ [kPa] \\ 0.00 \\ 9.70 \\ 15.58 \\ 20.89 \\ 26.47 \end{array} $	5.1.00 $\sigma_y$ [kPa] 0.00 2.08 3.36 4.33 5.26	$\lambda_x$ : $\lambda_x$ [-]  1.000  1.006  1.013  1.019  1.025	off-x $ \frac{\sigma_x}{[kPa]} $ 0.00 8.78 14.45 19.82 25.66	σ <sub>y</sub> [kPa] 0.00 6.80 10.71 14.15 17.83	$\lambda_x$ : $\lambda_x$ [-]  1.000  1.006  1.013  1.019  1.025	equi-biax $\lambda_y = 1.10$ $\sigma_x$ [kPa] 0.00 9.96 15.61 21.62 28.56	σ <sub>y</sub> [kPa] 0.00 9.96 15.61 21.62 28.56	$\lambda_x$ : $\lambda_y$ [-]  1.000  1.006  1.013  1.019  1.025	off-y $\lambda_{y} = 1.05$ $\sigma_{x}$ [kPa] $0.00$ $6.80$ $10.71$ $14.15$ $17.83$	: 1.10 $\sigma_y$ [kPa]  0.00 8.78 14.45 19.82 25.66	$\lambda_x$ : $\lambda_y$ [-]  1.000 1.006 1.013 1.019 1.025	strip-y $ \frac{\lambda_{y} = 1.00}{\sigma_{x}} $ [kPa] $ 0.00 2.08 3.36 4.33 5.26$	σ <sub>y</sub> [kPa 0.00 9.70 15.5 20.8 26.4 32.2
$\lambda_x$ : $\lambda_x$ [-]  1.000 1.006 1.013 1.019 1.025 1.031	strip-x $ \frac{\sigma_x}{[kPa]} $ 0.00 9.70 15.58 20.89 26.47 32.24	.: 1.00 $\sigma_y$ [kPa] 0.00 2.08 3.36 4.33 5.26 6.31	$\lambda_x$ : $\lambda_x$ [-]  1.000  1.006  1.013  1.019  1.025  1.031	$\begin{aligned} & \text{off-x} \\ & \lambda_y = 1.10 \\ & \sigma_x \\ & \text{[kPa]} \\ & 0.00 \\ & 8.78 \\ & 14.45 \\ & 19.82 \\ & 25.66 \\ & 31.86 \end{aligned}$	σ <sub>y</sub> [kPa] 0.00 6.80 10.71 14.15 17.83 21.74 25.78 30.97	$\lambda_x$ : $\lambda_x$ [-]  1.000  1.006  1.013  1.019  1.025  1.031	equi-biax $\lambda_y = 1.10$ $\sigma_x$ [kPa] 0.00 9.96 15.61 21.62 28.56 36.47	0.00 9.96 15.61 21.62 28.56 36.47	$\lambda_x$ : $\lambda_y$ [-]  1.000  1.006  1.013  1.019  1.025  1.031	$off-y$ $\lambda_y = 1.05$ $\sigma_x$ [kPa] $0.00$ $6.80$ $10.71$ $14.15$ $17.83$ $21.74$	: 1.10 $\sigma_y$ [kPa]  0.00 8.78 14.45 19.82 25.66 31.86	$\lambda_x$ : $\lambda_y$ [-]  1.000 1.006 1.013 1.019 1.025 1.031	strip-y $ \frac{\sigma_x}{[kPa]} $ 0.00 2.08 3.36 4.33 5.26 6.31	σ <sub>y</sub> [kPa 0.00 9.70 15.5 20.8 26.4 32.2 38.3 45.4
$\lambda_x$ : $\lambda_x$ [-]  1.000  1.006  1.013  1.019  1.025  1.031  1.038  1.044  1.050	strip-x $\begin{array}{l} \delta_{y} = 1.10 \\ \delta_{x} \\ \text{[kPa]} \\ 0.00 \\ 9.70 \\ 15.58 \\ 20.89 \\ 26.47 \\ 32.24 \\ 38.30 \\ \end{array}$	.: 1.00 $\sigma_y$ [kPa] 0.00 2.08 3.36 4.33 5.26 6.31 7.32	$\lambda_x$ : $\lambda_x$ [-]  1.000 1.006 1.013 1.019 1.025 1.031 1.038	$\begin{aligned} & \text{off-x} \\ & \lambda_y = 1.10 \\ & \sigma_x \\ & \text{[kPa]} \\ & 0.00 \\ & 8.78 \\ & 14.45 \\ & 19.82 \\ & 25.66 \\ & 31.86 \\ & 38.95 \end{aligned}$	1.05 $\sigma_y$ [kPa] 0.00 6.80 10.71 14.15 17.83 21.74 25.78	$\lambda_x$ : $\lambda_x$ [-]  1.000 1.006 1.013 1.019 1.025 1.031 1.038	equi-biax $\lambda_y = 1.10$ $\sigma_x$ [kPa] 0.00 9.96 15.61 21.62 28.56 36.47 45.83	0.00 9.96 15.61 21.62 28.56 36.47 45.83	$\lambda_x$ : $\lambda_y$ [-]  1.000 1.006 1.013 1.019 1.025 1.031 1.038	$off-y$ $\lambda_y = 1.05$ $\sigma_x$ [kPa] $0.00$ $6.80$ $10.71$ $14.15$ $17.83$ $21.74$ $25.78$	: 1.10	$\lambda_x$ : $\lambda_y$ [-]  1.000 1.006 1.013 1.019 1.025 1.031 1.038	strip-y $ \frac{\sigma_x}{[kPa]} $ 0.00 2.08 3.36 4.33 5.26 6.31 7.32	σ <sub>y</sub> [kPa 0.00 9.70 15.5 20.8 26.4 32.2 38.3 45.4 53.1
$\lambda_x$ : $\lambda_x$ [-]  1.000  1.006  1.013  1.019  1.025  1.031  1.038  1.044  1.050	$\begin{array}{c} strip-x \\ \hline \\ \lambda_y = 1.10 \\ \hline \\ \\ \\ \\ \\ \\ \\ \\ \\ \\ \\ \\ \\ \\ \\ \\ \\ $	σ <sub>y</sub> [kPa] 0.00 2.08 3.36 4.33 5.26 6.31 7.32 8.44	$\lambda_x$ : $\lambda_x$ [-]  1.000 1.006 1.013 1.019 1.025 1.031 1.038 1.044	$\begin{aligned} & \text{off-x} \\ \lambda_y &= 1.10 : \\ \sigma_x \\ & \text{[kPa]} \\ 0.00 \\ 8.78 \\ 14.45 \\ 19.82 \\ 25.66 \\ 31.86 \\ 38.95 \\ 47.91 \end{aligned}$	σ <sub>y</sub> [kPa] 0.00 6.80 10.71 14.15 17.83 21.74 25.78 30.97	$\lambda_x$ : [-]  1.000 1.006 1.013 1.019 1.025 1.031 1.038 1.044	equi-biax $\lambda_y = 1.10$ $\sigma_x$ [kPa] 0.00 9.96 15.61 21.62 28.56 36.47 45.83 58.50	σ <sub>y</sub> [kPa] 0.00 9.96 15.61 21.62 28.56 36.47 45.83 58.50	$\lambda_x$ : $\lambda_y$ [-]  1.000 1.006 1.013 1.019 1.025 1.031 1.038 1.044	$\begin{aligned} & \text{off-y} \\ \lambda_y &= 1.05 \\ & \sigma_x \\ & \text{[kPa]} \\ & 0.00 \\ & 6.80 \\ & 10.71 \\ & 14.15 \\ & 17.83 \\ & 21.74 \\ & 25.78 \\ & 30.97 \end{aligned}$	31.86 38.95 47.91	$\lambda_x$ : $\begin{array}{c} \lambda_y \\ [-] \\ 1.000 \\ 1.006 \\ 1.013 \\ 1.019 \\ 1.025 \\ 1.031 \\ 1.038 \\ 1.044 \end{array}$	$\begin{array}{c} strip-y \\ \hline \\ \\ \\ \\ \\ \\ \\ \\ \\ \\ \\ \\ \\ \\ \\ \\ \\ $	σ <sub>y</sub> [kPa 0.00 9.70 15.5 20.8 26.4 32.2 38.3 45.4
$\lambda_x$ : $\lambda_x$ [-] 1.000 1.006 1.013 1.019 1.025 1.031 1.038 1.044 1.050 1.056	strip-x $ \frac{\lambda_y = 1.10}{\sigma_x} $ [kPa] $ 0.00 9.70 15.58 20.89 26.47 32.24 38.30 45.41 53.15$	5 1.00    or of the first section of the first sect	$\lambda_x$ : $\begin{bmatrix} \lambda_x \\ - \end{bmatrix}$ 1.000 1.006 1.013 1.019 1.025 1.031 1.038 1.044 1.050	$\begin{array}{c} \text{off-x} \\ \lambda_y = 1.10 : \\ \sigma_x \\ \text{[kPa]} \\ 0.00 \\ 8.78 \\ 14.45 \\ 19.82 \\ 25.66 \\ 31.86 \\ 38.95 \\ 47.91 \\ 58.33 \end{array}$	σ <sub>y</sub> [kPa] 0.00 6.80 10.71 14.15 17.83 21.74 25.78 30.97 37.14	$\lambda_x$ : $\begin{bmatrix} \lambda_x \\ - \end{bmatrix}$ 1.000 1.006 1.013 1.019 1.025 1.031 1.038 1.044 1.050	equi-biax $\lambda_y = 1.10$ $\sigma_x$ [kPa] 0.00 9.96 15.61 21.62 28.56 36.47 45.83 58.50 73.30	5. 1.10 $\sigma_y$ [kPa] 0.00 9.96 15.61 21.62 28.56 36.47 45.83 58.50 73.30	$\begin{array}{c} \lambda_x:\\ \lambda_y\\ [-]\\ 1.000\\ 1.006\\ 1.013\\ 1.019\\ 1.025\\ 1.031\\ 1.038\\ 1.044\\ 1.050\\ \end{array}$	$\begin{array}{c} \text{off-y} \\ \lambda_y = 1.05 \\ \hline \sigma_x \\ \text{[kPa]} \\ \hline 0.00 \\ 6.80 \\ 10.71 \\ 14.15 \\ 17.83 \\ 21.74 \\ 25.78 \\ 30.97 \\ 37.14 \\ \end{array}$	: 1.10	$\lambda_x$ : $\lambda_y$ [-] 1.000 1.006 1.013 1.019 1.025 1.031 1.038 1.044 1.050	strip-y $\lambda_y = 1.00$ $\sigma_x$ [kPa] $0.00$ $2.08$ $3.36$ $4.33$ $5.26$ $6.31$ $7.32$ $8.44$ $9.83$	σ <sub>y</sub> [kPa 0.00 9.70 15.5 20.8 26.4 32.2 38.3 45.4 53.1
$\lambda_x$ : $\lambda_x$ [-]  1.000  1.006  1.013  1.019  1.025  1.031  1.038	strip-x $ \frac{\lambda_y = 1.10}{\sigma_x} $ [kPa] $ 0.00 9.70 15.58 20.89 26.47 32.24 38.30 45.41 53.15 62.09$	5. 1.00 To y [kPa] 0.00 2.08 3.36 4.33 5.26 6.31 7.32 8.44 9.83 11.48	$\lambda_x$ : [-] 1.000 1.006 1.013 1.019 1.025 1.038 1.044 1.050 1.056	$\begin{array}{c} \text{off-x} \\ \lambda_y = 1.10 \\ \hline \sigma_x \\ \text{[kPa]} \\ \hline 0.00 \\ 8.78 \\ 14.45 \\ 19.82 \\ 25.66 \\ 31.86 \\ 38.95 \\ 47.91 \\ 58.33 \\ 70.30 \\ \end{array}$	1.05  o <sub>y</sub> [kPa]  0.00 6.80 10.71 14.15 17.83 21.74 25.78 30.97 37.14 44.19	$\lambda_x$ : [-] 1.000 1.006 1.013 1.019 1.025 1.038 1.044 1.050 1.056	equi-biax $\lambda_y = 1.10$ $\sigma_x$ [kPa] 0.00 9.96 15.61 21.62 28.56 36.47 45.83 58.50 73.30 91.43	5. 1.10 $\sigma_y$ [kPa] 0.00 9.96 15.61 21.62 28.56 36.47 45.83 58.50 73.30 91.43	$\begin{array}{c} \lambda_x:\\ \lambda_y\\ [-]\\ 1.000\\ 1.006\\ 1.013\\ 1.019\\ 1.025\\ 1.031\\ 1.038\\ 1.044\\ 1.050\\ 1.056\\ \end{array}$	$off-y$ $\lambda_y = 1.05$ $\sigma_x$ [kPa] $0.00$ $6.80$ $10.71$ $14.15$ $17.83$ $21.74$ $25.78$ $30.97$ $37.14$ $44.19$	: 1.10	$\lambda_x$ : $\lambda_y$ [-] 1.000 1.006 1.013 1.019 1.025 1.031 1.038 1.044 1.050 1.056	strip-y $\lambda_y = 1.00$ $\sigma_x$ [kPa] 0.00 2.08 3.36 4.33 5.26 6.31 7.32 8.44 9.83 11.48	$\sigma_y$ [kPa 0.00 9.70 15.5 20.8 26.4 32.2 38.3 45.4 53.1 62.0
$\lambda_x$ : $\lambda_x$ [-]  1.000 1.006 1.013 1.019 1.025 1.031 1.038 1.044 1.050 1.056 1.063 1.069	$\begin{array}{c} \text{strip-x} \\ \vdots \\ \lambda_y = 1.10 \\ \\ \sigma_x \\ \text{[kPa]} \\ 0.00 \\ 9.70 \\ 15.58 \\ 20.89 \\ 26.47 \\ 32.24 \\ 38.30 \\ 45.41 \\ 53.15 \\ 62.09 \\ 72.81 \\ \end{array}$	σ <sub>y</sub> [kPa] 0.00 2.08 3.36 4.33 5.26 6.31 7.32 8.44 9.83 11.48 13.81	$\lambda_x$ : $\lambda_x$ [-]  1.000 1.006 1.013 1.019 1.025 1.031 1.038 1.044 1.050 1.056 1.063	off-x $ \frac{\sigma_x}{\rho_x} = 1.10 \pm 0.00 $ 8.78 14.45 19.82 25.66 31.86 38.95 47.91 58.33 70.30 84.18	σ <sub>y</sub> [kPa] 0.00 6.80 10.71 14.15 17.83 21.74 25.78 30.97 37.14 44.19 52.68	$\lambda_x$ : $\lambda_x$ [-]  1.000 1.006 1.013 1.019 1.025 1.031 1.038 1.044 1.050 1.056 1.063	equi-biax $\lambda_y = 1.10$ $\sigma_x$ [kPa] 0.00 9.96 15.61 21.62 28.56 36.47 45.83 58.50 73.30 91.43 113.37	σ <sub>y</sub> [kPa] 0.00 9.96 15.61 21.62 28.56 36.47 45.83 58.50 73.30 91.43 113.37	$\lambda_x$ : $\lambda_y$ [-]  1.000 1.006 1.013 1.019 1.025 1.031 1.038 1.044 1.050 1.056 1.063	$\begin{array}{c} \text{off-y} \\ \lambda_y = 1.05 \\ \hline \sigma_x \\ \text{[kPa]} \\ 0.00 \\ 6.80 \\ 10.71 \\ 14.15 \\ 17.83 \\ 21.74 \\ 25.78 \\ 30.97 \\ 37.14 \\ 44.19 \\ 52.68 \\ \end{array}$	: 1.10	$\lambda_x$ : $\lambda_y$ [-] 1.000 1.006 1.013 1.019 1.025 1.031 1.038 1.044 1.050 1.056 1.063	strip-y $\lambda_y = 1.00$ $\sigma_x$ [kPa] 0.00 2.08 3.36 4.33 5.26 6.31 7.32 8.44 9.83 11.48 13.81	σ <sub>y</sub> [kPa 0.00 9.70 15.5 20.8 26.4 32.2 38.3 45.4 53.1 62.0 72.8
$\lambda_x$ : $\lambda_x$ [-]  1.000 1.006 1.013 1.019 1.025 1.031 1.038 1.044 1.050 1.056 1.063	$\begin{array}{c} \text{strip-x} \\ \vdots \\ \lambda_y = 1.10 \\ \\ \sigma_x \\ \text{[kPa]} \\ 0.00 \\ 9.70 \\ 15.58 \\ 20.89 \\ 26.47 \\ 32.24 \\ 38.30 \\ 45.41 \\ 53.15 \\ 62.09 \\ 72.81 \\ 85.34 \\ \end{array}$	σ <sub>y</sub> [kPa] 0.00 2.08 3.36 4.33 5.26 6.31 7.32 8.44 9.83 11.48 13.81 16.47	$\lambda_x$ : $\lambda_x$ [-]  1.000 1.006 1.013 1.019 1.025 1.031 1.038 1.044 1.050 1.056 1.063 1.069	$\begin{array}{c} \text{off-x} \\ \lambda_y = 1.10 \\ \hline \sigma_x \\ \text{[kPa]} \\ \hline 0.00 \\ 8.78 \\ 14.45 \\ 19.82 \\ 25.66 \\ 31.86 \\ 38.95 \\ 47.91 \\ 58.33 \\ 70.30 \\ 84.18 \\ 101.18 \\ \end{array}$	σ <sub>y</sub> [kPa] 0.00 6.80 10.71 14.15 17.83 21.74 25.78 30.97 37.14 44.19 52.68 62.96	$\lambda_x$ : $\lambda_x$ [-]  1.000 1.006 1.013 1.019 1.025 1.031 1.038 1.044 1.050 1.056 1.063 1.069	equi-biax $\lambda_y = 1.10$ $\sigma_x$ [kPa] 0.00 9.96 15.61 21.62 28.56 36.47 45.83 58.50 73.30 91.43 113.37 138.85	σ <sub>y</sub> [kPa] 0.00 9.96 15.61 21.62 28.56 36.47 45.83 58.50 73.30 91.43 113.37 138.85	$\lambda_x$ : $\lambda_y$ [-]  1.000 1.006 1.013 1.019 1.025 1.031 1.038 1.044 1.050 1.056 1.063 1.069	$\begin{array}{c} \text{off-y} \\ \lambda_y = 1.05 \\ \hline \sigma_x \\ \text{[kPa]} \\ 0.00 \\ 6.80 \\ 10.71 \\ 14.15 \\ 17.83 \\ 21.74 \\ 25.78 \\ 30.97 \\ 37.14 \\ 44.19 \\ 52.68 \\ 62.96 \\ \end{array}$	: 1.10	$\lambda_{x}$ : $\lambda_{y}$ [-] 1.000 1.006 1.013 1.019 1.025 1.031 1.038 1.044 1.050 1.056 1.063 1.069	strip-y $\lambda_y = 1.00$ $\sigma_x$ [kPa] 0.00 2.08 3.36 4.33 5.26 6.31 7.32 8.44 9.83 11.48 13.81 16.47	σ <sub>y</sub> [kPa 0.00 9.70 15.5 20.8 26.4 32.2 38.3 45.4 53.1 62.0 72.8 85.3
$\lambda_x$ : $\lambda_x$ [-]  1.000 1.006 1.013 1.019 1.025 1.031 1.038 1.044 1.050 1.056 1.063 1.069 1.075	$\begin{array}{c} \text{strip-x} \\ \vdots \\ \lambda_y = 1.10 \\ \\ \sigma_x \\ \text{[kPa]} \\ 0.00 \\ 9.70 \\ 15.58 \\ 20.89 \\ 26.47 \\ 32.24 \\ 38.30 \\ 45.41 \\ 53.15 \\ 62.09 \\ 72.81 \\ 85.34 \\ 100.14 \\ \end{array}$	σ <sub>y</sub> [kPa] 0.00 2.08 3.36 4.33 5.26 6.31 7.32 8.44 9.83 11.48 13.81 16.47 19.79	$\lambda_x$ : $\lambda_x$ [-]  1.000 1.006 1.013 1.019 1.025 1.031 1.038 1.044 1.050 1.056 1.063 1.069 1.075	$\begin{array}{c} \text{off-x} \\ \lambda_y = 1.10 \\ \hline \sigma_x \\ \text{[kPa]} \\ \hline 0.00 \\ 8.78 \\ 14.45 \\ 19.82 \\ 25.66 \\ 31.86 \\ 38.95 \\ 47.91 \\ 58.33 \\ 70.30 \\ 84.18 \\ 101.18 \\ 121.49 \\ \end{array}$	σ <sub>y</sub> [kPa] 0.00 6.80 10.71 14.15 17.83 21.74 25.78 30.97 37.14 44.19 52.68 62.96 75.30	$\lambda_x$ : $\lambda_x$ [-] 1.000 1.006 1.013 1.019 1.025 1.031 1.038 1.044 1.050 1.056 1.063 1.069 1.075	equi-biax $\lambda_y = 1.10$ $\sigma_x$ [kPa] 0.00 9.96 15.61 21.62 28.56 36.47 45.83 58.50 73.30 91.43 113.37 138.85 170.42	σ <sub>y</sub> [kPa] 0.00 9.96 15.61 21.62 28.56 36.47 45.83 58.50 73.30 91.43 113.37 138.85 170.42	$\lambda_x$ : $\lambda_y$ [-]  1.000 1.006 1.013 1.019 1.025 1.031 1.038 1.044 1.050 1.056 1.063 1.069 1.075	$\begin{array}{c} \text{off-y} \\ \lambda_y = 1.05 \\ \hline \sigma_x \\ \text{[kPa]} \\ \hline 0.00 \\ 6.80 \\ 10.71 \\ 14.15 \\ 17.83 \\ 21.74 \\ 25.78 \\ 30.97 \\ 37.14 \\ 44.19 \\ 52.68 \\ 62.96 \\ 75.30 \\ \end{array}$	: 1.10	$\lambda_x$ : $\lambda_y$ [-] 1.000 1.006 1.013 1.019 1.025 1.031 1.038 1.044 1.050 1.056 1.063 1.069 1.075	strip-y $\lambda_y = 1.00$ $\sigma_x$ [kPa] $0.00$ 2.08 3.36 4.33 5.26 6.31 7.32 8.44 9.83 11.48 13.81 16.47 19.79	1: 1.05 σ <sub>y</sub> [kPa 0.00 9.70 15.5 20.8 26.4 32.2 38.3 45.4 53.1 62.0 72.8 85.3 100.
$\lambda_x$ : $\lambda_x$ [-]  1.000 1.006 1.013 1.019 1.025 1.031 1.038 1.044 1.050 1.056 1.063 1.069 1.075 1.081	$\begin{array}{c} \text{strip-x} \\ \hline \sigma_x \\ \text{[kPa]} \\ \hline 0.00 \\ 9.70 \\ 15.58 \\ 20.89 \\ 26.47 \\ 32.24 \\ 38.30 \\ 45.41 \\ 53.15 \\ 62.09 \\ 72.81 \\ 85.34 \\ 100.14 \\ 117.90 \\ \end{array}$	σ <sub>y</sub> [kPa] 0.00 2.08 3.36 4.33 5.26 6.31 7.32 8.44 9.83 11.48 13.81 16.47 19.79 23.78	$\lambda_x$ : $\lambda_x$ [-] 1.000 1.006 1.013 1.019 1.025 1.031 1.038 1.044 1.050 1.056 1.063 1.069 1.075 1.081	$\begin{array}{c} \text{off-x} \\ \lambda_y = 1.10 : \\ \sigma_x \\ \text{[kPa]} \\ 0.00 \\ 8.78 \\ 14.45 \\ 19.82 \\ 25.66 \\ 31.86 \\ 38.95 \\ 47.91 \\ 58.33 \\ 70.30 \\ 84.18 \\ 101.18 \\ 121.49 \\ 146.91 \\ \end{array}$	σ <sub>y</sub> [kPa] 0.00 6.80 10.71 14.15 17.83 21.74 25.78 30.97 37.14 44.19 52.68 62.96 75.30 90.74	$\lambda_x$ : $\lambda_x$ [-] 1.000 1.006 1.013 1.019 1.025 1.031 1.038 1.044 1.050 1.066 1.063 1.069 1.075 1.081	$\begin{array}{l} \text{equi-biax} \\ \lambda_y = 1.10 \\ \hline \sigma_x \\ \text{[kPa]} \\ \hline 0.00 \\ 9.96 \\ 15.61 \\ 21.62 \\ 28.56 \\ 36.47 \\ 45.83 \\ 58.50 \\ 73.30 \\ 91.43 \\ 113.37 \\ 138.85 \\ 170.42 \\ 211.22 \\ \end{array}$	σ <sub>y</sub> [kPa] 0.00 9.96 15.61 21.62 28.56 36.47 45.83 58.50 73.30 91.43 113.37 138.85 170.42 211.22	$\begin{array}{c} \lambda_x:\\ \lambda_y\\ [-]\\ 1.000\\ 1.006\\ 1.013\\ 1.019\\ 1.025\\ 1.031\\ 1.038\\ 1.044\\ 1.050\\ 1.056\\ 1.063\\ 1.069\\ 1.075\\ 1.081\\ \end{array}$	$\begin{array}{c} \text{off-y} \\ \lambda_y = 1.05 \\ \hline \sigma_x \\ \text{[kPa]} \\ \hline 0.00 \\ 6.80 \\ 10.71 \\ 14.15 \\ 17.83 \\ 21.74 \\ 25.78 \\ 30.97 \\ 37.14 \\ 44.19 \\ 52.68 \\ 62.96 \\ 75.30 \\ 90.74 \\ \end{array}$	3.30 (8.18 to 1.18 to	$\lambda_x$ : $\lambda_y$ [-] 1.000 1.006 1.013 1.019 1.025 1.031 1.038 1.044 1.050 1.056 1.063 1.069 1.075 1.081	strip-y $\lambda_y = 1.00$ $\sigma_x$ [kPa] $0.00$ 2.08 3.36 4.33 5.26 6.31 7.32 8.44 9.83 11.48 13.81 16.47 19.79 23.78	σ <sub>y</sub> [kPa 0.00 9.70 15.5 20.8 26.4 32.2 38.3 45.4 53.1 62.0 72.8 85.3 100.

where the stiffness-like parameters are  $a_1=91.24$  kPa,  $\mu_1=3794$  kPa,  $a_2=3.31$  kPa,  $a_3=5.30$  kPa, and the nonlinearity parameters are  $b_1=0.17$ ,  $b_2=127.20$ ,  $b_3=94.68$ . Fig. 7 illustrates the discovered two-fiber model along with the biaxial test data. It highlights four different terms in four characteristic colors and quantifies the goodness of all 15 fits in terms of the  $R^2$  values. The individual stress-stretch plots suggest that the discovered model performs fairly well on the experiments in the 0/90 orientation, but performs poorly on the strip-x experiment in the -45/+45 orientation, where it significantly under-predicts the x-stress and overpredicts the y-stress. This reduces the mean  $R^2$  value across all tests to 0.7573.

Additionally, we train a subset of the network in Fig. 3 with only anisotropic terms. To do this, we constrain the weights of all eight isotropic terms to equal zero,  $w_1, \ldots, w_8 = 0$ . We again use  $L_{0.5}$  regularization with a regularization parameter  $\alpha = 0.001$  and use all data for training. Fig. 8 shows the discovered two-fiber model with no isotropic terms. The network discovers two anisotropic terms, both are the exponential linear Weiss terms [63], one in the fourth warp invariant  $L_{4w}$  and one in the fourth

shute invariant  $I_{4s}$ ,

$$\psi = \frac{1}{2}a_1 \left[ \exp(b_1[I_{4w} - 1]) - 1 \right] / b_1 - \frac{1}{2}a_1 \left[ I_{4w} - 1 \right]$$
  
+  $\frac{1}{2}a_2 \left[ \exp(b_2[I_{4s} - 1]) - 1 \right] / b_2 - \frac{1}{2}a_2 \left[ I_{4s} - 1 \right]$ 

with the two stiffness-like parameters  $a_1=2.998$  kPa,  $a_2=9.811$  kPa, and the two nonlinearity parameters  $b_1=21.07$ ,  $b_2=12.63$ . Notably, the fit of this model is extremely poor. The mean  $R^2$  value across all tests is as low as 0.5104, and five tests have  $R^2$  values of zero. We conclude that the orthotropic two-fiber model with no isotropic terms fails to accurately describe the behavior of the mesh.

Next, instead of sparsifying the model and reducing the number of terms with  $L_{0.5}$  regularization, we use  $L_0$  regularization to identify the best one- and two-term models by sampling all 14 single terms and all 91 pairs of two terms and minimizing the mean squared error of the 105 models. Fig. 9 shows the minimized loss for all 105 combination of terms with the one-term models on the diagonale and the two-term models off the diagonale. For the two-fiber architecture, the best-in-class two-term model consists of one isotropic term, the exponential linear first invariant  $I_1$  Demiray [8],

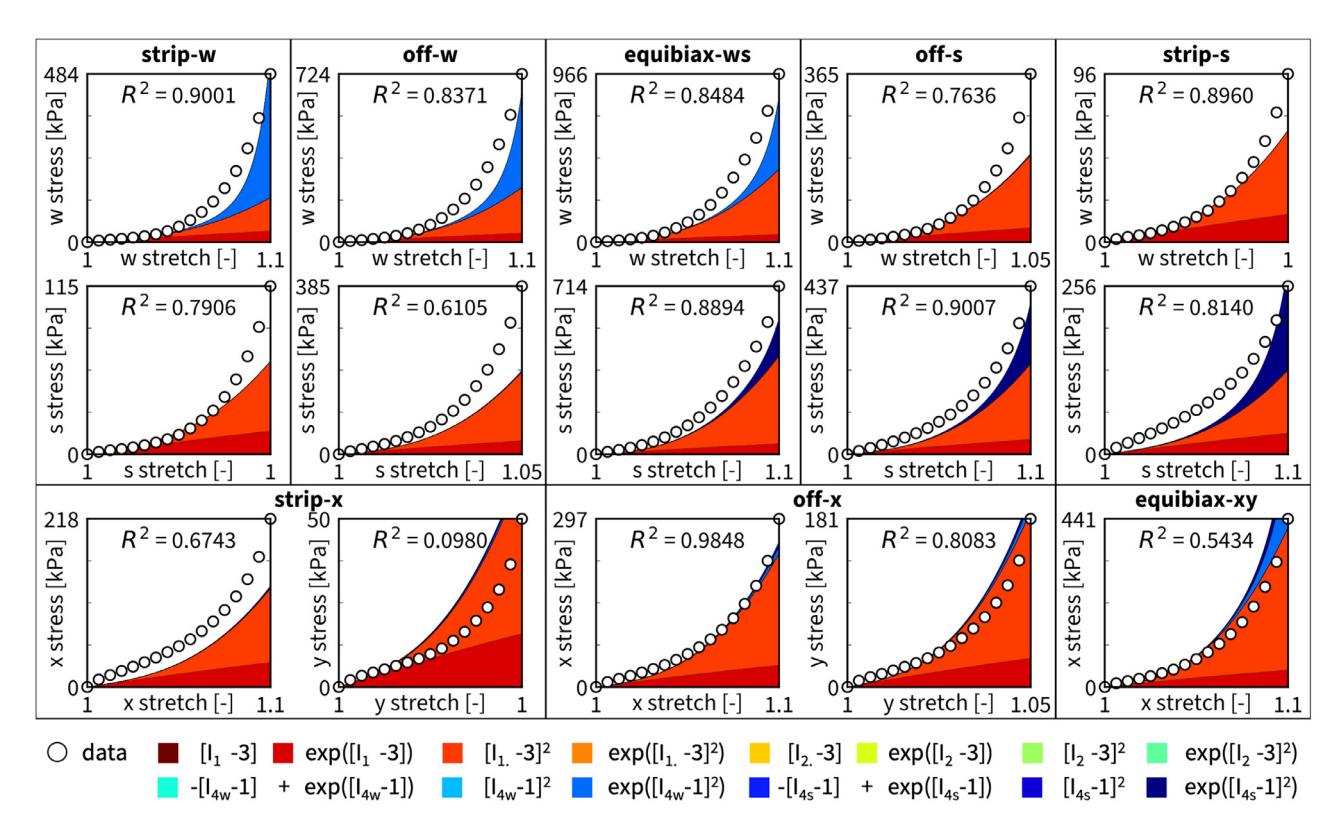


**Fig. 7.** Discovered two-fiber model and biaxial test data. We train the two-fiber constitutive neural network from Fig. 3 on all 15 data sets and sparsify the discovered model with  $L_{0.5}$  regularization. The network discovers a four-term model with two isotropic terms and two anisotropic terms, which we plot in their characteristic colors. The  $R^2$  values suggest that the discovered model performs decent on most of the tests in the 0/90 orientation, but performs particularly poorly on the strip-x experiment in the -45/+45 orientation where it underpredicts the x-stress and overpredicts the y-stress. The mean  $R^2$  value across all tests is 0.7573.

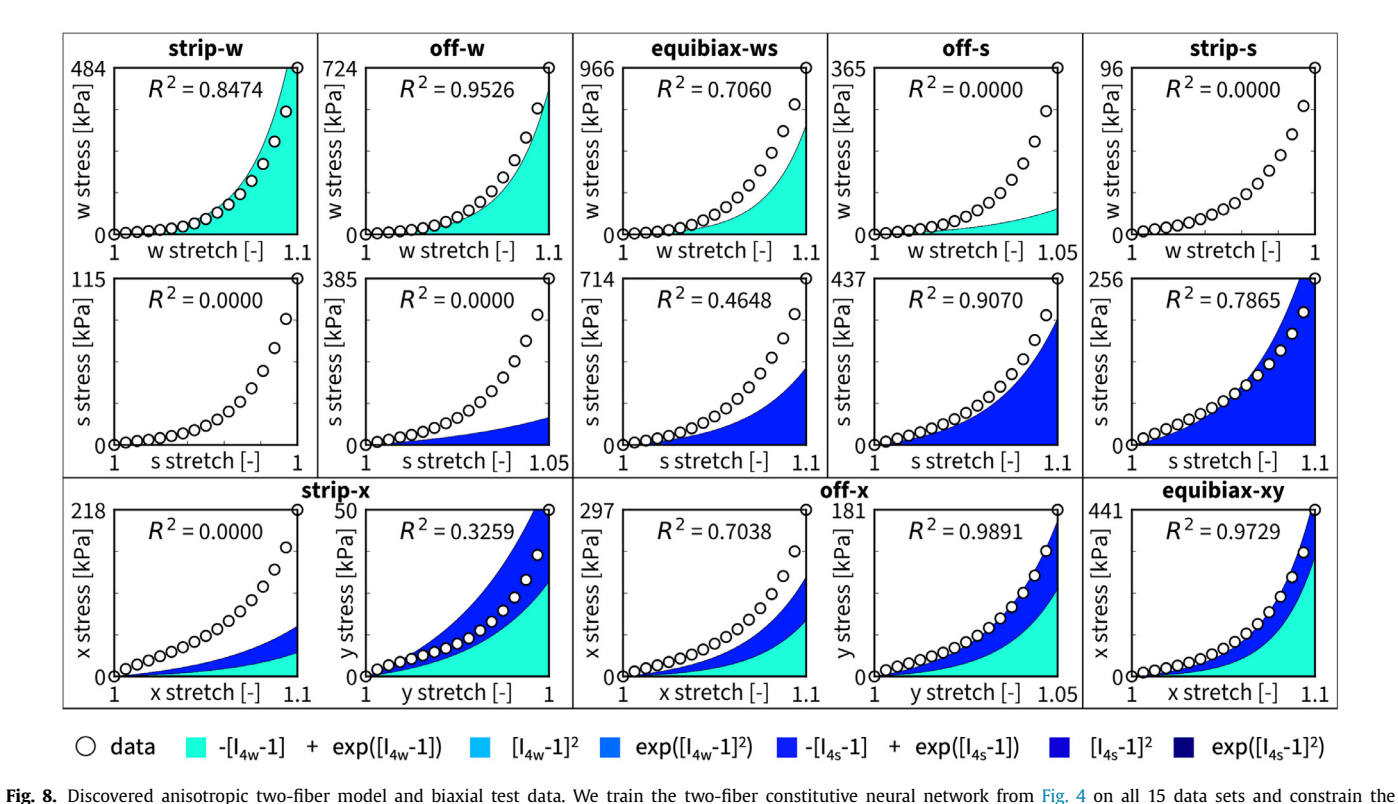
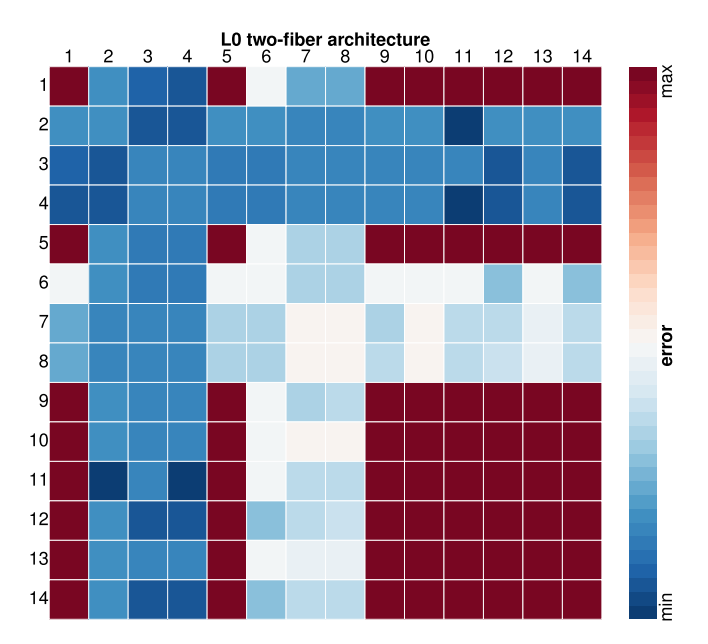


Fig. 8. Discovered anisotropic two-iner model and blaxial test data. We train the two-iner constitutive neural network from Fig. 4 on all 15 data sets and constrain the weights for the isotropic terms to be zero. The network discovers a two-term model with one term that is a function of the fourth warp invariant  $I_{4w}$  and one that is a function of the fourth shute invariant  $I_{4s}$ , which we plot in their characteristic colors. The  $R^2$  values suggest that the discovered model performs poorly on most tests, with  $R^2$  values of zero for several tests. The mean  $R^2$  value across all tests is 0.5104.



**Fig. 9.** Best-in-class one- and two-term two-fiber models. All models are made up of 14 functional building blocks: linear, exponential linear, quadratic, and exponential quadratic terms of the first invariant  $I_1$ , rows and columns 1 to 4, of the second invariant  $I_2$ , rows and columns 5 to 8, of the fourth warp invariant  $I_{4w}$  rows and columns 9 to 11, and of the fourth shute invariant  $I_{4s}$  rows and columns 12 to 14. The color code indicates the mean squared error of the 14 one-term models on the diagonale, and of the 91 two-term models on the off-diagonale, ranging from dark blue, best fit, to dark red, worst fit. (For interpretation of the references to colour in this figure legend, the reader is referred to the web version of this article.)

and one anisotropic term, the exponential quadratic fourth warp invariant  $I_{4w}$  Holzapfel term [16],

$$\psi = \frac{1}{2}a_1 \left[ \exp(b_1[I_1 - 3]) - 1 \right] / b_1 + \frac{1}{2}a_2 \left[ \exp(b_2[I_{4w} - 1]^2) - 1 \right] / b_2,$$

with the two stiffness-like parameters  $a_1 = 25.20$  kPa and  $a_2 = 0.40$  kPa, and the two nonlinearity parameters  $b_1 = 17.30$  and  $b_2 = 127.30$ , and achieves a training loss of 0.077. Strikingly, while the data suggest that the mesh is highly anisotropic, the models with only anisotropic terms perform the worst.

### 3.3. Three-fiber architecture

Second, we train the full network using the three-fiber architecture in Fig. 4. Again, we initialize the model parameters randomly and train the network without any regularization. Then, we use these trained parameters to re-initialize the parameters and train the network using  $L_{0.5}$  regularization with a regularization parameter  $\alpha=0.001$ . We use data from all experiments for training. Fig. 10 shows the discovered model, with the contributions of each discovered stress term in a different color. The network discovers three non-zero terms, one is the exponential quadratic first invariant  $I_1$  Holzapfel term [16], and two are the exponential linear fourth warp and shute invariants  $I_{4w}$  and  $I_{4s_I}$  and  $I_{4s_{II}}$  Weiss terms [63],

$$\psi = \frac{1}{2}a_{1}[\exp(b_{1}[I_{1}-3]^{2})-1]/b_{1}$$

$$+ \frac{1}{2}a_{2}[\exp(b_{2}[I_{4w}-1])-1]/b_{2} - \frac{1}{2}a_{2}[I_{4w}-1]$$

$$+ \frac{1}{2}a_{3}[\exp(b_{3}[I_{4s_{1}}-1])-1]/b_{3} - \frac{1}{2}a_{3}[I_{4s_{1}}-1]$$

where the stiffness-like parameters are  $a_1 = 2427$  kPa,  $a_2 = 0.16$  kPa,  $a_3 = 81.77$  kPa, and the nonlinearity parameters are  $b_1 = 0.51$ ,  $b_2 = 37.65$ ,  $b_3 = 4.78$ . Fig. 10 shows the discovered three-fiber model along with the biaxial test data. Similar to the two-fiber model in Fig. 7, the three-fiber model performs fairly well on

the experiments in the 0/90 orientation. However, in contrast to the two-fiber model, the three-fiber model also performs well on the strip-x experiment in the +45/-45 orientation and achieves an  $R^2$  of 0.98 in the x-direction and 0.93 in the y-direction compared to the two-fiber model with only 0.67 in the x-direction and 0.10 in the y-direction. Its mean  $R^2$  value across all tests is 0.8614.

Additionally, we train a subset of the network in Fig. 4 with only anisotropic terms. Again, we constrain the weights of all eight isotropic terms to equal zero,  $w_1, \ldots, w_8 = 0$ , use  $L_{0.5}$  regularization with  $\alpha = 0.001$ , and use all data for training. Fig. 11 shows the discovered three-fiber model with no isotropic terms. Similar to the two-term case, the network discovers two anisotropic terms, both are exponential linear Weiss terms [63], one in the fourth warp invariant  $I_{4w}$  and one in the fourth shute invariants  $I_{4s_I}$  and  $I_{4s_{II}}$ ,

$$\psi = \frac{1}{2}a_1 \left[ \exp(b_1[I_{4w} - 1]) - 1 \right] / b_1 - \frac{1}{2}a_1 \left[ I_{4w} - 1 \right]$$
  
+  $\frac{1}{2}a_2 \left[ \exp(b_2(I_{4S_{1,1}} - 1]) - 1 \right] / b_2 - \frac{1}{2}a_2 \left[ I_{4S_{1,1}} - 1 \right]$ 

with the two stiffness-like parameters,  $a_1 = 1.26$  kPa,  $a_2 = 28.93$  kPa, and the two nonlinearity parameters  $b_1 = 24.55$ ,  $b_2 = 7.20$ . Notably, the anisotropic three-fiber model in Fig. 11 with a mean  $R^2$  value of 0.8199 provides a much better fit to the data than the anisotropic two-fiber model in Fig. 8 with a mean  $R^2$  value of 0.5104, and, without any isotropic terms, performs almost as good as the three-fiber model in Fig. 10 with a mean  $R^2$  value of 0.8614.

Finally, we use  $L_0$  regularization to identify the best one- and two-term models by sampling all 14 single terms and all 91 pairs of two terms. Fig. 12 shows the minimized loss for all 105 combination of terms. The first eleven terms in the three-fiber architecture are identical to the first eleven terms in the two-fiber architecture, which means the only difference between Figs. 9 and 12 are the last three rows and columns associated with the shute invariants  $I_{4s_{II}}$  and  $I_{4s_{II}}$ . Interestingly, for the three-fiber architecture, the best-in-class two-term model is identical to the discovered non-isotropic model with two exponential linear Weiss terms [63], one in the fourth warp invariant  $I_{4w}$  and one in the fourth shute invariants  $I_{4s_{II}}$  and  $I_{4s_{II}}$ ,

$$\psi = \frac{1}{2}a_1 \left[ \exp(b_1[I_{4w} - 1]) - 1 \right] / b_1 - \frac{1}{2}a_1 \left[ I_{4w} - 1 \right]$$
  
+  $\frac{1}{2}a_2 \left[ \exp(b_2(I_{4s_{11}} - 1]) - 1 \right] / b_2 - \frac{1}{2}a_2 \left[ I_{4s_{11}} - 1 \right]$ 

with the two stiffness-like parameters,  $a_1 = 1.26$  kPa,  $a_2 = 28.93$  kPa, and the two nonlinearity parameters  $b_1 = 24.55$ ,  $b_2 = 7.20$ , and a training loss of 0.04. Strikingly, of all possible one- and two-term models, the best model characterizes the warp knitted mesh without any isotropic terms, and is exclusively made up of exponential linear terms of the squared stretches along the microstructural directions of the mesh.

### 3.4. Training and testing

To demonstrate that our discovered models have predictive capability beyond the data used in training, we train the network using a subset of the data and use the remaining data to test model performance. Yet, rather than randomly partitioning the available data into a training and test sets, we choose each of the tests to either be entirely part of the training set or test set. This is because the observations within a single test are highly correlated, and a constitutive model is most useful if it is capable of accurately predicting the resulting stress when the applied deformation takes a form that differs from the training data. We train the network with the three-fiber architecture from Fig. 4 using four different training sets: the first training set consists of all experiments, the second consists of only experiments in the 0/90 orientation; the third consists of only experiments in the +45/-45 orientation;

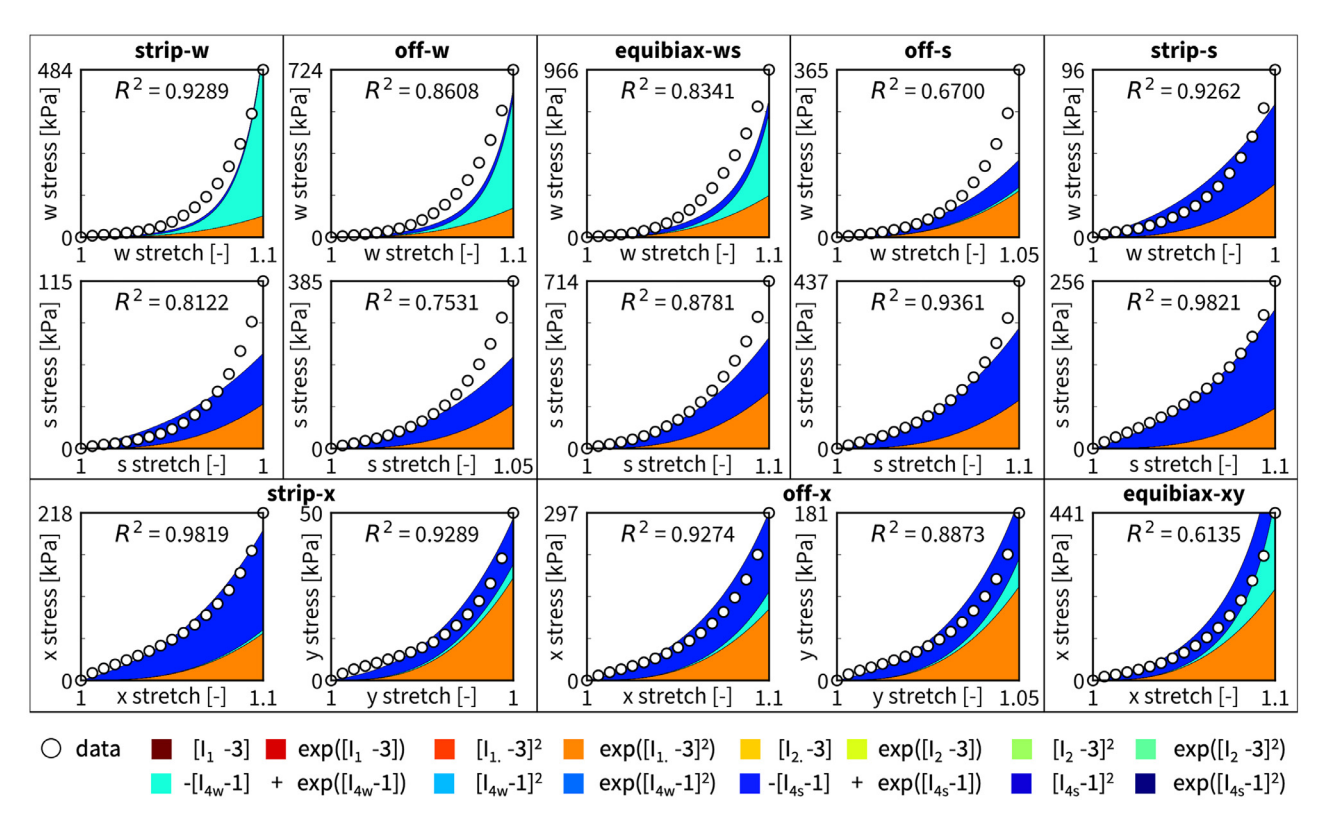


**Fig. 10.** Discovered three-fiber model and biaxial test data. We train the three-fiber constitutive neural network from Fig. 4 on all 15 data sets and sparsify the discovered model with  $L_{0.5}$  regularization. The network discovers a three-term model with one isotropic term and two anisotropic terms, which we plot in their characteristic colors. The  $R^2$  values suggest that the discovered model performs well on all fifteen tests. The mean  $R^2$  value across all tests is 0.8614.

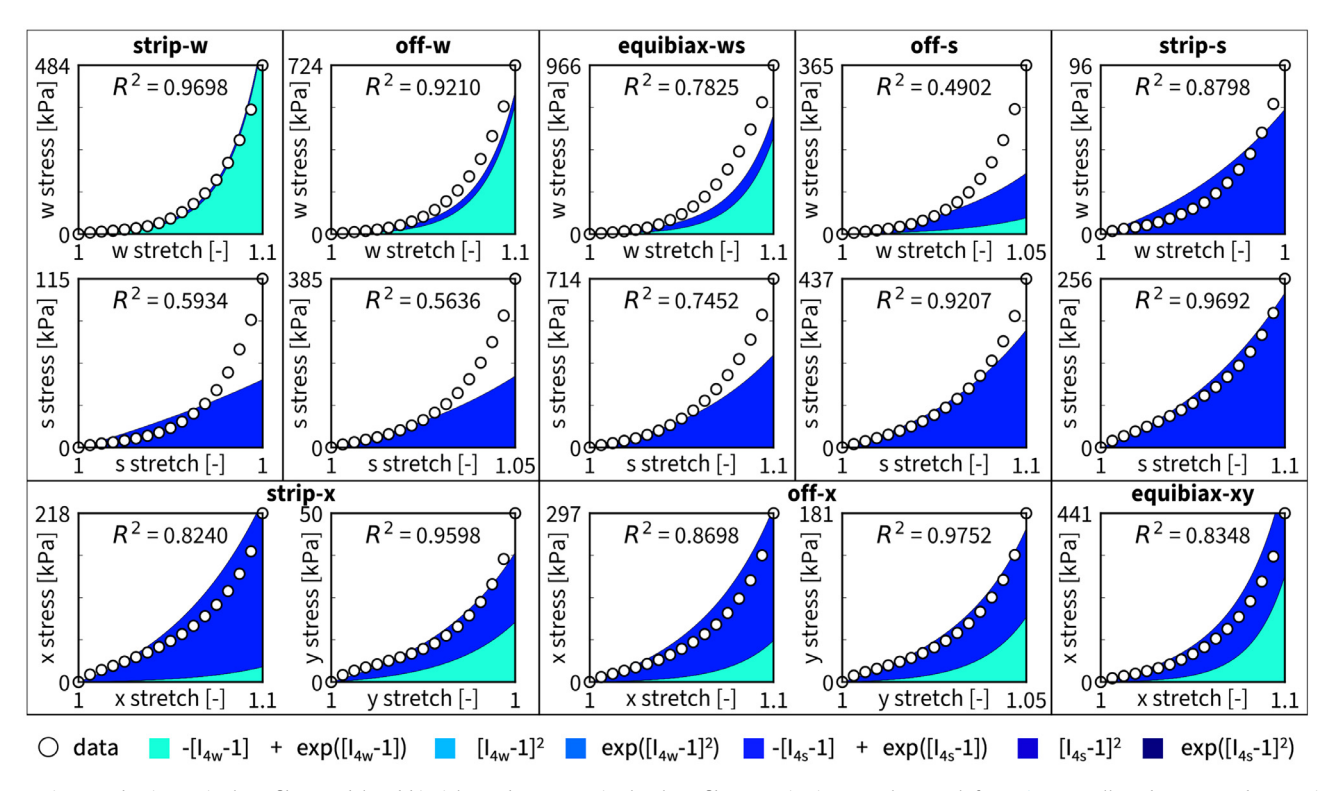


**Fig. 11.** Discovered anisotropic three-fiber model and biaxial test data. We train the three-fiber constitutive neural network from **Fig. 4** on all 15 data sets and constrain the weights for the isotropic terms to be zero. The network discovers a two-term model with one term that is a function of the fourth warp invariant  $I_{4w}$  and one that is a function of the fourth shute invariants  $I_{4s_1}$  and  $I_{4s_{11}}$ , which we plot in their characteristic colors. The model that is discovered is very similar to the optimal two-term model shown in **Fig. 12**. The  $R^2$  values suggest that, even without isotropic terms, the discovered model performs well across all fifteen tests. The mean  $R^2$  value across all tests is 0.8199.

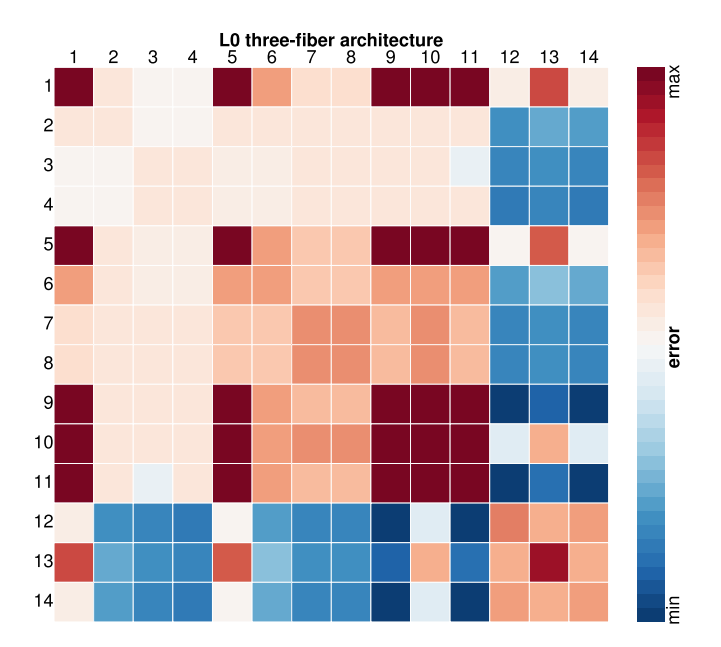


**Fig. 12.** Best-in-class one- and two-term three-fiber models. All models are made up of 14 functional building blocks: linear, exponential linear, quadratic, and exponential quadratic terms of the first invariant  $I_1$ , rows and columns 1 to 4, of the second invariant  $I_2$ , rows and columns 5 to 8, of the fourth warp invariant  $I_{4w}$  rows and columns 9 to 11, and of the fourth shute invariants  $I_{4s_p}$  and  $I_{4s_p}$  rows and columns 12 to 14. The color code indicates the mean squared error of the 14 one-term models on the diagonale, and of the 91 two-term models on the off-diagonale, ranging from dark blue, best fit, to dark red, worst fit. (For interpretation of the references to colour in this figure legend, the reader is referred to the web version of this article.)

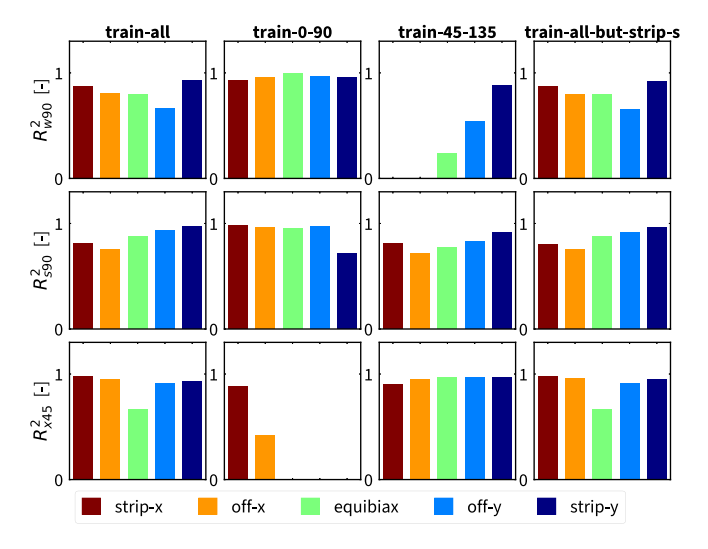


**Fig. 13.** Performance of three-fiber network for four different training sets. The columns represent the four training sets: data from only the 0/90 orientation, data from only the +45/-45 orientation, all data, and all data except the strip-s data in the 0/90 orientation. The rows represent the coefficients of determination of the warp stress in the 0/90 orientation, the shute stress in the 0/90 orientation, and the x stress in the +45/-45 orientation. To accurately predict the stress in all loading conditions, the training set must include data from both the 0/90 and +45/-45 orientations.

and the fourth consists of all experiments except strip-shute loading in the 0/90 orientation. Fig. 13 shows the resulting coefficient of determination  $R^2$  for each stress-stretch curve when training the model on each of these four training sets. The figure illustrates that it is insufficient to train exclusively on the tests in the 0/90 orientation or on tests in the +45/-45 orientation; data from both orientations are essential to fully understand the constitutive behavior

of our mesh. Notably, the model performance on the strip-shute tests when trained with all data except strip-shute is remarkably similar to the model performance when trained on all data. This suggests that the model is capable of extrapolating to unseen data, and shows that it does not overfit the training data.

#### 4. Discussion

Synthetic meshes have unique mechanical properties, which make them ideal candidates for many engineering and medical applications. The objective of this study was to provide insights into the mechanical signature of synthetic meshes using an integrative approach that combines biaxial testing and automated model discovery. We prototyped this approach using a 0.5 mm thick warp knitted surgical mesh of extruded polypropylene. We tested the mesh in two different orientations, the 0/90 orientation with the loading axis aligned with the warp direction, and the -45/+45 orientation with the loading axis inclined by 45 degrees to the warp direction. We compared two families of microstructural models, a two-fiber model with a warp direction  $\vec{w}$  and one orthogonal shute direction  $\vec{s}$ , and a three-fiber model with a warp direction  $\vec{w}$  and two symmetrical shute directions  $\vec{s_l}$  and  $\vec{s_{II}}$  inclined by 60 degrees. Our study confirms our intuition that knitted meshes display a remarkable initial flexibility, a pronounced nonlinear stiffening, and an extreme anisotropy. Beyond these expected observations, it also reveals several exciting features of polypropylene meshes.

Exponential linear fourth invariant terms dominate the constitutive response of polypropylene meshes. Throughout this study, we pursued different approaches to discover the best model and parameters to characterize textile structures. We trained a full neural network with fourteen independent terms and a subset of the network with only the six anisotropic terms, both for the two- and three-fiber model, with pronounced directions inclined by either 90 or 60 degrees. This allows us to discover the best model and parameters out of  $2^{14} = 16,384$  and  $2^6 = 64$  possible combinations of terms. Strikingly, one term reoccured consistently through automated model discovery: the exponential linear fourth invariant term,  $\frac{1}{2} a [\exp(b[I_4 - 1]) - 1]/b - \frac{1}{2} a[I_4 - 1]$ . Originally proposed for soft biological tissues [63], this term is ideally suited to characterize the remarkable initial flexibility of the virgin mesh and the pronounced nonlinear stiffening as the loops of the mesh tighten upon loading. Of all four discovered models in Figs. 7, 8, 10, and 11, three prominently feature this exponential linear fourth invariant term, both in the warp and shute directions  $I_{4w}$ and  $I_{4s}$ , highlighted through the turquoise and blue colors. We confirm the dominance of these two terms with an entirely independent best-in-class modeling study in Figs. 9 and 12 that also identifies the turquoise and blue terms to make up the best-in-class two-term model out of 91 possible two-term models, both for the two- and three-fiber microstructure. Interestingly, the full network model in Fig. 10 with a mean  $R^2$  value of 0.8614 performs only marginally better than the reduced network model in Fig. 11 with a mean  $R^2$  value of 0.8199. This suggest that we can confidently use the discovered two-term fourth-invariant model that features no isotropic terms to characterize the ultra-anisotropic nature of polypropylene meshes.

Mixed invariant terms are critical to characterize the interaction of the warp and shute directions. To systematically explore the importance of the mixed invariant  $I_{8ws}$ , we studied two different microstructural models. Fig. 2 illustrates their two distinct microstructures, which represent the loops of the mesh as through warp direction  $\vec{w}$  and the underlap through a single orthogonal shute direction  $\vec{s}$  or two shoot directions  $\vec{s}_l$  and  $\vec{s}_{ll}$ , symmetrically offset by 60 degrees [21]. A direct comparison of the performance of our discovered two-fiber and three-fiber models in Figs. 7 and

10 suggests that incorporating detailed microstructural information along all three directions is critical for model accuracy [57]. In Fig. 7, we can see that the two-fiber model significantly underpredicts the x-stress and over-predicts the y-stress for the strip-x experiment in the +45/-45 orientation. To show that this error is a direct consequence of the two-fiber model, we take a closer look at the anisotropic stress contributions. In particular, when the strain energy is not a function of  $I_{8ws}$ , the contribution of the anisotropic terms to the x- and y-stress in the +45/-45 orientation is  $P_{xx}^{ani}$  =  $\lambda_{x}(\partial\psi/\partial I_{4w}+\partial\psi/\partial I_{4s})$  and  $P_{yy}^{ani}=\lambda_{y}(\partial\psi/\partial I_{4w}+\partial\psi/\partial I_{4s})$ , thus,  $P_{xx}^{ani}/P_{yy}^{ani}=\lambda_x/\lambda_y$ . At maximum strip-x loading in the +45/-45 orientation, the stretches are  $\lambda_x = 1.1$  and  $\lambda_y = 1.0$ , such that  $\lambda_x/\lambda_y =$ 1.1, and the stresses are  $P_{xx}^{ani} = 219$  kPa and  $P_{yy}^{ani} = 50$  kPa, such that  $P_{xx}^{ani}/P_{yy}^{ani}=4.38$ . We can directly see this discrepancy in Fig. 8, where the discovered model has an R<sup>2</sup> value of zero for the xstress in strip-x loading in the +45/-45 orientation. This suggests that an appropriate model for warp knitted meshes should indeed be a function of the mixed invariant  $I_{8ws}$ . If the strain energy  $\psi$  is a function of the mixed invariant  $I_{8ws}$  [34], the derivative  $\partial \psi / \partial I_{8ws}$  contributes a positive component to  $P_{xx}^{\rm ani}$  and a negative component to  $P_{yy}^{\rm ani}$ . For positive mixed invariants,  $\partial \psi / \partial I_{8ws} > 0$ , such that  $P_{xx}^{\rm ani} \geq P_{yy}^{\rm ani}$ , and thus  $P_{xx}^{\rm ani}/P_{yy}^{\rm ani} \geq \lambda_x/\lambda_y$ , which is what we observe in Table 2. This observation is in line with several previous studies that have acknowledged the importance of the mixed invariant for double-fiber reinforced nonlinear elastic materials [36].

Understanding the shear response is critical to model textile structures. Even with an appropriate constitutive neural network that is informed by the microstructure of the mesh, our inability to measure shear strain in biaxial loading [10] results in a loss of model accuracy in certain loading modes. Most obviously, when comparing Figs. 7 and 10, we notice that the model generally under-predicts the shute and warp stresses in the 0/90 orientation, and over-predicts the x- and y-stresses in the +45/-45 orientation. When taking a closer look at the states of maximum deformation in equibiaxial loading, we see that when  $\lambda_w =$  $\lambda_s = \lambda = 1.1$  in the 0/90 orientation, the invariants and mixed invariants are identical to when  $\lambda_x=\lambda_y=\lambda=1.1$  in the +45/-45 orientation. In both cases,  $I_1=2\lambda^2+\lambda^{-4}$  and  $I_2=2\lambda^{-2}+\lambda^4$ and  $I_{4w}=I_{4s}=\lambda^2$  and  $I_{8ws}=0$ . As a result, the strain energy  $\psi$  and its partial derivatives are identical in both cases. Thus,  $P_{ww}^{ani}=2\lambda\,\partial\psi/\partial I_{4w}$  and  $P_{ss}^{ani}=2\lambda\,\partial\psi/\partial I_{4s}$  and  $P_{xx}^{ani}=\lambda\,(\partial\psi/\partial I_{4w}+1)$  $\partial \psi/\partial I_{4s}+\partial \psi/\partial I_{8ws}).$  Since  $I_{8ws}=0$  and  $\psi$  is an even function of  $I_{8ws}$ , by symmetry, we know that  $\partial \psi / \partial I_{8ws} = 0$ , and thus,  $P_{ww} +$  $P_{\rm SS} = 2 P_{\rm XX}$ . However, looking at the data,  $P_{\rm WW} + P_{\rm SS} = 996$  kPa + 714 kPa = 1710 kPa, while  $2P_{xx} = 884$  kPa. This contradiction is triggered by our assumptions in Eqs. (5) and (16) that the deformation remains homogeneous and shear free at all times, such that the deformation gradient F remains diagonal, Ff = diag  $\{\lambda_x, \lambda_y, \lambda_x^{-1} \lambda_y^{-1}\}$ . This condition holds for samples loaded in biaxial tension, if their microstructure is symmetric about the two loading directions. While this is true for isotropic materials in general, and it holds for orthotropic materials in the 0/90 configuration, it does not always hold for orthotropic materials in the +45/-45 configuration: Loading non-symmetrically mounted orthotropic materials in biaxial tension tests may actually result in non-zero shear strains [52]. Since the CellScale BioTester 5000 grips the material using slender tines that are stiff in tension but compliant in bending, a more accurate boundary condition would be that the axial stretches are equal to the values measured by the device, and the shear stresses are equal to zero. In this case, the shear strains would be non-zero and would take the values that minimize the strain energy given the prescribed axial stretches in the two loading directions. This change would decrease the predicted strain energy in the +45/-45 orientation, while leaving the strain energy in the 0/90 orientation unchanged. As a result, we would expect  $2P_{XX} < P_{WW} + P_{SS}$ , which is indeed what we observe in Table 2. To accurately incorporate this effect, we would need to measure the shear strain, which the CellScale BioTester 5000 does not directly control or measure.

Our networks reliably extrapolate to unseen data. Our study confirms, that with an appropriate microstructural representation, our constitutive neural network discovers generalizable anisotropic constitutive models, provided that we use training data from both the 0/90 and +45/-45 orientations. From the goodness-of-fit bar plots in Fig. 13, it is clear that training on only data from the 0/90 orientation results in inaccurate model predictions in the +45/-45 orientation, and vice versa. This result is not surprising since certain characteristics of the material are only active and visible in one of the two orientations. In particular, in the +45/-45 orientation, by symmetry  $I_{4w} = I_{4s}$  for all loading states, which means that it is not possible to independently probe the  $I_{4w}$  and  $I_{4s}$  terms. Similarly, in the 0/90 orientation,  $I_{8ws} = 0$  for all loading states of the two-fiber models, so we cannot measure the effect of  $I_{8ws}$ on the stress. Thus, the training data must consist of data from both orientations for the model to robustly predict stresses under all possible conditions. Another interesting observation from Fig. 13 is that, when training on all the available data except the strip-shute data in the 0/90 configuration, the discovered model achieves similar  $R^2$  values for the training and test data when compared to the model trained on all the data. This suggests that our model is not overfitting the data, and that when trained on a subset of data from both orientations, it is able to accurately predict the stresses for deformation states that we do not use in training.

**From model discovery to generative material design**. Our constitutive neural networks in Figs. 3 and 4 solve the forward problem to *discover the best model and parameters* that describe a given material, in our case the textile microstructure. Inversely, we could use our constitutive neural networks and solve the inverse problem to *discover the best material* for a given model and parameters, for example, a desired directional stiffness.

Both problems combined represent a classical example for bidirectional learning where layer-wise relevance propagation can provide insight into the forward problem of model discovery, whereas layer-wise relevance backpropagation can provide insight into the inverse problem of material discovery [2]. Alternatively, recent advances in structural feature representation and generative neural networks now allow us to more efficiently design materials with tailored properties and functions. In materials science, generative neural networks are currently gaining immense popularity in the design of solid-state crystalline materials [65], where the features that represent the crystalline microstructure are the atom type, the lattice vectors, and the atomic coordinates in the Euclidian space [43]. In textile science, these features naturally translate into yarn type, varn angles, and knot or loop coordinates. Two popular and emerging models for inverse material design are variational autoencoders and generative adversarial networks [64]. A variational autoencoder consists of an encoder that transforms the input sample feature vector into the latent space where it generates the latent space vector z from a normal distribution  $N(\sigma, \mu)$  and a decoder that reconstructs the sample from the given hidden distribution. A generative adversarial network consists of a generator that generates samples from random noise variables and a discriminator that determines whether a sample is valid or invalid. Fig. 14 compares the material design process with our constitutive neural network for forward model discovery and inverse material discovery with these two popular generative neural networks, variational autoencoders and generative adversarial networks. Adapting neural network modeling to design programmable textile metamaterials with tunable properties and functions would open unique oppor-

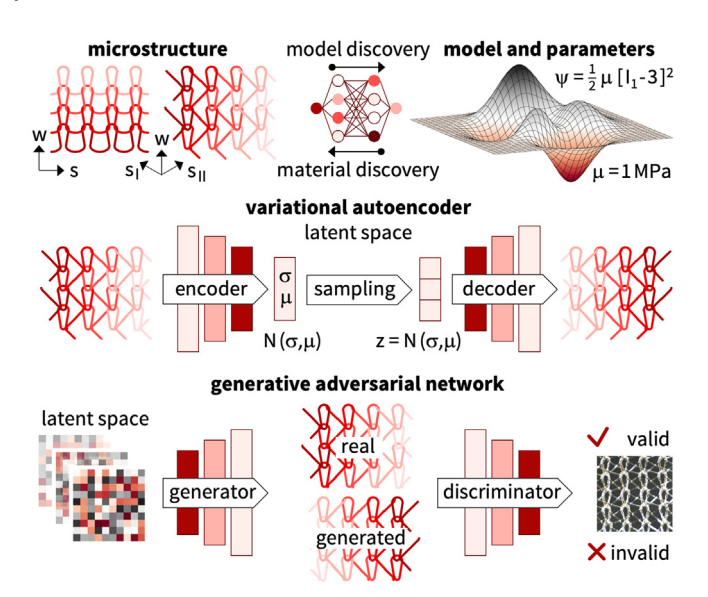


**Fig. 14.** Material design with generative neural networks. Constitutive neural networks solve the forward problem to *discover models and parameters* for given microstructures, and could solve the inverse problem to *discover materials* for given models and parameters. A *variational autoencoder* for generative material design combines an *encoder* to transform the input sample feature vector into the latent space where it generates the latent space vector z from a normal distribution  $N(\sigma, \mu)$  and a *decoder* to reconstruct the sample from the given hidden distribution. A *generative adversarial network* for generative material design combines a *generator* to generate samples from random noise variables and a *discriminator* to determine whether a sample is valid or invalid.

tunities in textile science with possible applications to wearable devices, stretchable electronics, and smart fabrics.

Limitations and future directions. Our study presents a first step in characterizing textile structures using automated model discovery. Here we prototype this approach for a single warp knitted polypropylene mesh. While our experience with other material types [27,28,30,48] suggests that our approach will generalize naturally to other textile structures-woven, werf knitted or warp knitted-our current study has a few limitations that point towards future research directions: First, our current study is limited to the hyperelastic regime. However, we have recorded separate loading and unloading data and expanding the model discovery process the inelastic regime using viscoelastic [62] or general inelastic [15] constitutive artificial neural networks would be the next logical step. Second, our study focuses on characterizing the twodimensional in-plane behavior or the fabric structure. Expanding it to a more physiological fully three-dimensional in- and out-ofplane characterization is conceptually possible, but would require additional tests, for example, the ball burst test that characterizes the indentation response of the fabric as a thin membrane [6]. Third, our biaxial test setup uses square samples mounted by tines or rakes [10]. Alternatively, we could have mounted the samples using clamps, and we plan to investigate the impact of different mounting techniques in a future study. Finally, our current study assumes a homogeneous shear free state. A possible future extension would be to quantify shear strains using full field data from digital image correlation [1] and embed model discovery within the solution of real boundary value problems with possibly heterogeneous stresses and stretches [11].

#### 5. Conclusion

Characterizing the mechanical properties of synthetic meshes is critical to understand their unique properties and functions. To date, identifying appropriate constitutive models for woven and

knitted textiles poses a critical barrier to mechanically tailoring and fine-tuning these structures to individual needs. Machinelearning approaches can discover anisotropic constitutive models from biaxial data; yet, existing approaches are limited to training data from a single mounting orientation. Here we show that this approach can result in superficial constitutive models that generalize poorly to unseen data. In contrast, the new approach we advocate here uses data from at least two different mounting orientations, and robustly discovers models that perform well during both training and testing. Importantly, our study shows that the accuracy of the discovered models is highly sensitive to an accurate representation of the microstructural architecture of the sample: Even if the textile fabric appears orthotropic at first glance, an accurate kinematic characterization of both warp and shute directions is critical to discover robust and reliable models. We demonstrate that these models are dominated by exponential linear fourth invariant terms that uniquely capture the remarkable initial flexibility, pronounced nonlinear stiffening, and extreme anisotropy of warp knitted polypropylene meshes. We anticipate that the tools we have developed here will generalize naturally to other textile fabrics-woven or knitted, weft knit or warp knit, with laid-in stitches or plain, polymeric or metallic-and, ultimately, will enable the robust discovery of anisotropic constitutive models for a wide variety of textile structures. Beyond discovering constitutive models, we envision to exploit automated model discovery as a novel strategy for the generative material design of wearable devices, stretchable electronics, and smart fabrics, as programmable textile metamaterials with tunable properties and functions.

### Data availability

Our source code, data, and examples are available at https://github.com/LivingMatterLab/CANN.

### **Declaration of competing interest**

The authors declare that they have no known competing financial interests or personal relationships that could have appeared to influence the work reported in this paper.

### **CRediT authorship contribution statement**

**Jeremy A. McCulloch:** Visualization, Validation, Software, Methodology, Investigation, Formal analysis, Data curation, Conceptualization. **Ellen Kuhl:** Writing – review & editing, Supervision, Conceptualization.

### Acknowledgments

This work was supported by the NSF Graduate Student Fellowship to Jeremy A. McCulloch and by the NSF CMMI Award 2320933 Automated Model Discovery for Soft Matter and by the ERC Advanced Grant 101141626 DISCOVER to Ellen Kuhl.

### References

- [1] S. Avril, M. Bonnet, A.S. Bretelle, M. Grediac, F. Hild, P. Ienny, F. Latourte, D. Lemosse, S. Pagano, E. Pagnacco, F. Pierron, Overview of identification methods of mechanical parameters based on full-field measurements, Exp. Mech. 48 (2008) 381–402.
- [2] S. Bach, A. Binder, G. Montavon, F. Klauschen, K.R. Müller, W. Samek, On pixel-wise explanations for non-linear classifier decisions by layer-wise relevance propagation, PLoS ONE 10 (2015). E0130140
- [3] K. Baylon, P. Rodriguez-Camarillo, A. Elias-Zuniga, J.A. Diaz-Elizondo, R. Gilkerson, K. Lozano, Past, present and future of surgical meshes: areview, Membranes 7 (2017) 47.

- [4] I. Bettermann, H. Löcken, C. Greb, T. Gries, A. Oses, J. Pauw, N. Maghaldadze, L. Datashvili, Review and evaluation of warp-knitted patterns for metal-based large deployable reflector surfaces, CEAS Space J. 15 (2023) 477–493.
- [5] S.L. Brunton, P.J. Proctor, J.N. Kutz, Discovering governing equations from data by sparse identification of nonlinear dynamical systems, Proc. Natl. Acad. Sci. 113 (2016) 3932–3937.
- [6] V. Civilini, V. Giacalone, A.L. Audenino, M. Terzini, A reliable and replicable test protocol for the mechanical evaluation of synthetic meshes, J. Mech. Behav. Biomed. Mater. 114 (2023) 105987.
- [7] E.B. Deerenberg, J. Verhelst, S.E.R. Hovius, J.F. Lange, Mesh expansion as the cause of bulging after abdominal wall hernia repair, Int. J. Surg. Case Rep. 28 (2016) 200–203.
- [8] H. Demiray, A note on the elasticity of soft biological tissues, J. Biomech. 5 (1972) 309–311.
- [9] S. Est, M. Roen, T. Chi, A. Simien, R.M. Castile, D.M. Thompson, J.A. Blatnik, C.R. Deeken, S.P. Lake, Multi-directional mechanical analysis of synthetic scaffolds for hernia repair, J. Mech. Behav. Biomed. Mater. 71 (2017) 43–53.
- [10] H. Fehervary, M. Smoljkic, J.V. Sloten, N. Famaey, Planar biaxial testing of soft biological tissue using rakes: a critical analysis of protocol and fitting process, J. Mech. Behav. Biomed. Mater. 61 (2016) 135–151.
- [11] M. Flaschel, S. Kumar, L. De Lorenzis, Unsupervised discovery of interpretable hyperelastic constitutive laws, Comput. Methods Appl. Mech. Eng. 381 (2021) 113852
- [12] J.N. Fuhg, R.E. Jones, N. Bouklas, Extreme sparsification of physics-augmented neural networks for interpretable model discovery in mechanics, Comput. Methods Appl. Mech. Eng. 426 (2024) 116973.
- [13] W. He, G. Cao, X. Gan, Y. Fan, B. Pei, X. Li, Evaluation methods for mechanical biocompatibility of hernia repair meshes: respective characteristics, application scope and future perspectives, J. Mater. Res. Technol. 13 (2021) 1826–1840.
- [14] T. Hastie, R. Tibshirani, J. Friedman, The Elements of Statistical Learning, second ed., 2009. Springer, New York.
- [15] H. Holthusen, L. Lamm, T. Brepols, S. Reese, E. Kuhl, Theory and implementation of inelastic constitutive artificial neural networks, Comput. Methods Appl. Mech. Eng. 428 (2024) 117063.
- [16] G.A. Holzapfel, T.C. Gasser, R.W. Ogden, A new constitutive framework for arterial wall mechanics and comparative study of material models, J. Elast. 61 (2000) 1–48.
- [17] G.A. Holzapfel, Nonlinear Solid Mechanics: A Continuum Approach to Engineering, John Wiley & Sons, Chichester, 2000.
- [18] J. Hu, B. Kumar, J. Lu, Handbood of Fibrous Materials, Wiley-VCH Verlag, Weinheim, Germany, 2000.
- [19] C. Jiang, K. Wang, Y. Liu, C. Zhang, B. Wang, Application of textile technology in tissue engineering: a review, Acta Biomater. 128 (2021) 60-76.
- [20] F. Kallinowski, Y. Ludwig, D. Gutjahr, C. Gerhard, H. Schulte-Hörmann, L. Krimmel, C. Lesch, K. Uhr, P. Lösel, S. Voss, V. Heuveline, M. Vollmer, J. Görich, R. Nessel, Biomechanical influences on mesh-related complications in incisional hernia repair, Front. Surg. 8 (2021) 763957.
- [21] Y. Kyosev, Topology-Based Modeling of Textile Structures and their Joint Assemblies. Principles, Algorithms and Limitations, Springer Nature Switzerland, 2019.
- [22] Y. Lanir, Y.C. Fung, Two-dimensional mechanical properties of rabbit skinll. experimental results, J. Biomech. 7 (1974) 171–182.
- [23] C. Lesch, R. Nessel, D. Adolf, M. Hukauf, F. Köckerling, F. Kallinowski, STRONGHOLD First-year results of biomechanically calculated abdominal wall repair: a propensity score matching, Hernia 28 (2024) 63–73.
- [24] A. Liberski, N. Ayad, D. Wojciechowska, D. Zieliska, M.H. Struszczyk, N. Latif, M. Yacoub, Knitting for heart valve tissue engineering, Global Cardiol. Sci. Pract. 31 (2016) 1–33.
- [25] K. Linka, M. Hillgartner, K.P. Abdolazizi, R.C. Aydin, M. Itskov, C.J. Cyron, Constitutive artificial neural networks: a fast and general approach to predictive data-driven constitutive modeling by deep learning, J. Comput. Phys. 429 (2021) 110010.
- [26] K. Linka, E. Kuhl, A new family of constitutive artificial neural networks towards automated model discovery, Comput. Methods Appl. Mech. Eng. 403 (2023) 115731.
- [27] K. Linka, S.R. St Pierre, E. Kuhl, Automated model discovery for human brain using constitutive artificial neural networks, Acta Biomater. 160 (2023) 134–151
- [28] K. Linka, A.B. Tepole, G.A. Holzapfel, E. Kuhl, Automated model discovery for skin: discovering the best model, data, and experiment, Comput. Methods Appl. Mech. Eng. 410 (2023) 116007.
- [29] L. Liu, P. Ma, Review on the performances and applications of mesh-fabrics, J. Ind. Text. 52 (2022) 128.
- [30] D. Martonova, M. Peirlinck, K. Linka, G.A. Holzapfel, S. Leyendecker, E. Kuhl, Automated model discovery for human cardiac tissue: discovering the best model and parameters, Comput. Methods Appl. Mech. Eng. 428 (2024) 117078.
- [31] M.M. Maurer, B. Röhrnbauer, A. Feola, J. Deprest, E. Mazza, Mechanical biocompatibility of prosthetic meshes: acomprehensive protocol for mechanical characterization, J. Mech. Behav. Biomed. Mater. 40 (2014) 42–58.
- [32] J.A. McCulloch, S.R. StPierre, K. Linka, E. Kuhl, On sparse regression, lp-regularization, and automated model discovery, Int. J. Numer. Methods Eng. 125 (2024), E7481
- [33] W.D. Meador, G.P. Sugerman, A.B. Tepole, M.K. Rausch, Biaxial mechanics of thermally denaturing skin, Acta Biomater. 140 (2022) 412–420.
- [34] A.V. Melnik, X. Luo, R.W. Ogden, A generalised structure tensor model for the mixed invariant i8, Int. J. Non Linear Mech. 107 (2018) 137148.

[35] A. Menzel, Frontiers in Inelastic Continuum Mechanics, Technical University of Kaiserslautern, 2007 Habilitation Thesis.

- [36] J. Merodio, R.W. Ogden, The influence of the invariant i8 on the stress-deformation and ellipticity characteristics of doubly fiber-reinforced non-linearly elastic solids, Int. J. Non Linear Mech. 41 (2006) 556–563.
- [37] I.H. Mondal, M. Islam, I. Haque, F. Ahmed, Natural, biodegradable, biocompatible and bioresorbable medical textile materials, in: Medical Textiles from Natural Resources, 2023, pp. 87–116.
- [38] A. Morch, L. Astruc, J.F. Witz, F. Lesaffre, P. Lecompte-Grosbras, D. Soulat, M. Brieu, Modeling of anisotropic hyperelastic heterogeneous knitted fabric reinforced composites, J. Mech. Phys. Solids 127 (2019) 47–61.
- [39] K. Nakano, V.L. Popov, Dynamic stiction without static friction: the role of friction vector rotation, Phys. Rev. E 102 (2020) 063001.
- [40] R. Nessel, T. Löffler, J. Rinn, F. Kallinowski, Three-year follow-up of the grip concept: an open, prospective observational registry study on biomechanically calculated abdominal wall repair for complex incisional hernias, Hernia 28 (2024) 913–924.
- [41] J.L. Ng, C.E. Collins, M.L.K. Tate, Engineering mechanical gradients in next generation biomaterials lessons learned from medical textile design, Acta Biomater. 56 (2017) 14–24.
- [42] S.W. Nienhuijs, C. Rosman, L.J.A. Strobbe, A. Wolff, R.P. Bleichrodt, An overview of the features influencing pain after inguinal hernia repair, Int. J. Surg. 6 (2008) 351–356.
- [43] H. Park, Z. Li, A. Walsh, Has generative artificial intelligence solved inverse material design? Matter 7 (2024) 2355–2367.
- [44] E.M. Parsons, T. Weerasooriya, S. Sarva, S. Socrate, Impact of woven fabric: experiments and mesostructure-based continuum-level simulations, J. Mech. Phys. Solids 58 (2010) 1995–2021.
- [45] M. Peirlinck, K. Linka, J.A. Hurtado, G.A. Holzapfel, E. Kuhl, Democratizing biomedical simulation through automated model discovery and a universal material subroutine, Comput. Mech. (2024), doi:10.1007/s00466-024-02515-y. in press
- [46] S.R. St Pierre, K. Linka, E. Kuhl, Principal-stretch-based constitutive neural networks autonomously discover a subclass of ogden models for human brain tissue, Brain Multiphys. 4 (2023) 100066.
- [47] S.R. StPierre, D. Rajasekharan, E.C. Darwin, K. Linka, M.E. Levenston, E. Kuhl, Discovering the mechanics of artificial and real meat, Comput. Methods Appl. Mech. Eng. 415 (2023) 116236.
- [48] S.R. St Pierre, E.C. Darwin, D. Adil, M.C. Aviles, A. Date, R.A. Dunne, Y. Lall, M.P. Vallecillo, V.A.P. Medina, K. Linka, M.E. Levenston, E. Kuhl, Got meat? The mechanical signature of plant-based and animal meat, BioRxiv (2024), doi:10. 1101/2024.04.25.591207.
- [49] M. Raissi, P. Perdikaris, G.E. Karniadakis, Physics-informed neural networks: a deep learning framework for solving forward and inverse problems involving nonlinear partial differential equations, J. Comput. Phys. 378 (2019) 686–707.
- [50] W. Renkens, Y. Kyosev, Geometry modelling of warp knitted fabrics with 3d form, Text. Res. J. 81 (2010) 437443.
- [51] B. Röhrnbauer, Y. Ozog, J. Eggerc, E. Werbrouck, J. Deprest, E. Mazza, Combined biaxial and uniaxial mechanical characterization of prosthetic meshes in a rabbit model, J. Biomech. 46 (2013) 1626–1632.
- [52] B. Röhrnbauer, E. Mazza, Uniaxial and biaxial mechanical characterization of a prosthetic mesh at different length scales, J. Mech. Behav. Biomed. Mater. 29 (2014) 7–19.
- [53] C.W. See, T. Kim, D. Zhu, Hernia mesh and hernia repair: a review, Eng. Regener. 1 (2020) 19–33.
- [54] M.P. Simons, M. Smietanski, H.J. Bonjer, R. Bittner, M. Miserez, T.J. Aufenacker, R.J. Fitzgibbons, P.K. Chowbey, H.M. Tran, R. Sani, F. Berrevoet, J. Bingener, T. Bisgaard, K. Bury, G. Campanelli, D.C. Chen, J. Conze, D. Cuccurullo, A.C. deBeaux, H.H. Eker, R.H. Fortelny, J.F. Gillion, B.J.v. Heuvel, W.W. Hope, L.N. Jorgensen, U. Klinge, F. Köckerling, J.F. Kukleta, I. Konate, A.L. Liem, D. Lomanto, M.J.A. Loos, M. Lopez-Cano, M.C. Misra, A. Montgomery, S. Morales-Conde, F.E. Muysoms, H. Niebuhr, P. Nordin, M. Pawlak, G.H. van Ramshorst, D.L. Sanders, N. Schouten, S. Smedberg, R.K.J. Simmermacher, S. Tumtavitikul, N.v. Veenendaal, D. Weyhe, A.R. Wijsmuller, The HerniaSurge Group, International guidelines for groin hernia management, Hernia 22 (2018) 1–165.
- [55] K. Singal, M.S. Dimitriyev, S.E. Gonzalez, A.P. Cachine, S. Quinn, E.A. Matsumoto, Programming mechanics in knitted materials, stitch by stitch, Nat. Commun. 15 (2024) 2622.
- [56] A.J.M. Spencer, Theory of invariants, in: A.C. Eringen (Ed.), Continuum Physics, volume 1, Academic Press, New York, 1971, pp. 239–353.
- [57] A.J.M. Spencer, A theory of viscoplasticity for fabric-reinforced composites, J. Mech. Phys. Solids 49 (2001) 2667–2687.
- [58] V. Tac, V.D. Sree, M.K. Rausch, A.B. Tepole, Data-driven modeling of the mechanical behavior of anisotropic soft biological tissues, Eng. Comput. 38 (2022) 4167–4182.
- [59] V. Tac, K. Linka, F.S. Costabal, E. Kuhl, A.B. Tepole, Benchmarking physics-informed frameworks for data-driven hyperelasticity, Comput. Mech. 73 (2024) 49–65
- [60] L.R.G. Treloar, Stresses and birefringence in rubber subjected to general homogeneous strain, Proc. Phys. Soc. 63 (1948) 135–144.
- [61] K.V. Linden, H. Fehervary, L. Maes, N. Famaey, An improved parameter fitting approach of a planar biaxial test including the experimental prestretch, J. Mech. Behav. Biomed. Mater. 134 (2022) 105389.
- [62] L.M. Wang, K. Linka, E. Kuhl, Automated model discovery for muscle using constitutive recurrent neural networks, J. Mech. Behav. Biomed. Mater. 145 (2023) 106021.

- [63] J.A. Weiss, B.N. Marker, S. Govindjee, Finite element implementation of incom-[63] J.A. Welss, B.N. Marker, S. Govinglee, Finite element implementation of incompressible, transversely isotropic hyperelasticity, Comput. Methods Appl. Mech. Eng. 135 (1996) 107–128.
  [64] D. Yan, A.D. Smith, C.C. Chen, Structure prediction and materials design with generative neural networks, Nat. Comput. Sci. 3 (2023) 572–584.
- [65] C. Zeni, R. Pinsler, D. Zügner, A. Fowler, M. Horton, X. Fu, S. Shysheya, J. Crabbe, L. Sun, J. Smith, B. Nguyen, H. Schulz, S. Lewis, C.W. Huang, Z. Lu, Y. Zhou, H. Yang, H. Hao, J. Li, R. Tomioka, T. Xie, MatterGen: a generative model for inorganic materials design, 2023. ArXiv, 2312.03687.